UNIVERSITA' DI PADOVA  FACOLTA' DI INGEGNERIA

Dipartimento di Ingegneria dell'Informazione

Scuola di Dottorato di Ricerca in Ingegneria dell'Informazione
Indirizzo: Bioingegneria

CICLO XXI

AUTOMATIC ANALYSIS OF CONFOCAL IMAGES OF THE CORNEA

Direttore della Scuola: Ch.mo Prof. Matteo Bertocco

Supervisore: Ch.mo Prof. Alfredo Ruggeri

Dottorando: Fabio Scarpa

Contents

Index:

Contents **i**
Index i
List of Figure iii
List of Table v

Sommario **vii**

Summary **ix**

1 Introduction **1**
1.1 Aim and Objectives 1
1.2 Outline of the thesis 3

2 The Cornea **5**
2.1 Eye anatomy 5
2.2 Corneal morphology 7
2.3 Corneal innervations 10
2.4 Confocal microscopy 11

3 Nerves Tracing **15**
3.1 Materials 15
3.2 Luminosity and contrast normalization 16
3.3 Seed points extraction 17
3.4 Bubble analysis 18
3.5 Tracing 20
3.5.1 Scan line analysis 20
3.5.2 Nerve profile selection 22
3.5.3 Scan line updating 23
3.6 The two-carabinieri technique 23
3.7 High-Pass filter 25
3.8 False nerve elimination 25
3.8.1 Keratocytes recognition 25
3.8.2 Internal and external area 26
3.9 Gabor filter 27
3.10 Performance evaluation 28
3.11 Conclusions 35
3.12 Further development 36

4 3D Reconstruction and Keratocyte Density Estimation 39
4.1 Materials 39
4.2 Image enhancement 40
4.2 Registration procedure 41
4.3 3D visualization 42
4.4 Keratocyte recognition 45
4.5 Keratocyte density 47
4.6 Performance evaluation 49
4.7 Conclusions 51

5 Cell Contour Detection 55
5.1 Materials 55
5.2 Illumination and contrast correction 56
5.3 Segmentation 57
5.3.1 Features selection 57
5.3.2 Artificial neural network training process 58
5.4 Automatic ROI selection 60
5.4.1 Entropy 60
5.4.2 Power Spectral Density 61
5.4.3 Entropy and Power Spectral Density interpolation 62
5.5 Post-processing 63
5.5.1 Contour completion 63
5.5.2 Split and merge 64
5.6 Performance evaluation 65

6 Conclusions 71
6.1 Achieving the Objectives 71
6.1.1 Nerves tracing 71
6.1.2 3D reconstruction and keratocyte density estimation 72
6.1.3 Cell contour detection 73
6.2 The way ahead 73

Bibliography 75

List of Figure:

Figure 1.1: Epithelium layer (containing the nerve fibers). 1
Figure 1.2: Stroma layer (containing the round-shaped keratocytes cell). 1

Figure 2.1 : Eye Anatomy. 5
Figure 2.2: The Cornea. 8
Figure 2.3: Reconstruction of corneal layers. 8
Figure 2.4: Superficial epithelium..... 10
Figure 2.5: Sub-epithelial nerve plexus. 10
Figure 2.6: Stroma..... 10
Figure 2.7: Endothelium. 10
Figure 2.8: Corneal innervations..... 11
Figure 2.9: Confocal microscope exam. 12
Figure 2.10: Confocal microscope arrangement. 13

Figure 3.1: Corneal sub-basal layer. 15
Figure 3.2: Original image and pre-processed normalized version. 17
Figure 3.3: Seed points extraction..... 18
Figure 3.4: Seed points before (a) and after (b) Hough transform..... 19
Figure 3.5: Step of the tracing..... 23
Figure 3.6: The two “carabinieri”. 24
Figure 3.7: Original image and high-pass filtered version..... 25
Figure 3.8: Internal and external area. 26
Figure 3.9: Graphic representation of Gabor filter..... 28
Figure 3.10: Original image and Gabor filtered version. 28
Figure 3.11: Scatter-plot..... 31
Figure 3.12: Scatter-plot..... 31
Figure 3.13: Scatter-plot..... 32
Figure 3.14: Bland-Altman plot. 32
Figure 3.15: Bland-Altman plot. 32
Figure 3.16: Bland-Altman plot. 32
Figure 3.17: Representative result of the nerve tracing technique..... 33
Figure 3.18: Representative result of the nerve tracing technique..... 33
Figure 3.19: Representative result of the nerve tracing technique..... 34
Figure 3.20: Scatter-plot..... 35
Figure 3.21: Bland-Altman. 35
Figure 3.22: All the images of a sequence containing nerves..... 36
Figure 3.23: original image and average version. 36
Figure 3.24: tracing performed on the original image and on the average image 37

Figure 4.1: Image of cornea stroma. 39
Figure 4.2: Sequence of images, from endothelium to epithelium 40
Figure 4.3: Original image and Pre-processed version. 41
Figure 4.4: Reconstructed stack 43
Figure 4.5: Images before (left) and after (right) interpolation. 44
Figure 4.6: Side view from y direction, in the x-z plane, 1114x1005 pixel. 44
Figure 4.7: Side view from x direction, in the y-z plane, 628x1005 pixel. 44
Figure 4.8: Side view from z direction, in the x-y plane, 628x1114 pixel. 45
Figure 4.9: 3D object. 45
Figure 4.10: Fixed ROI selection. 45
Figure 4.11: Keratocytes recognition: original image and enhanced version 46
Figure 4.12: Keratocytes recognition: morphological operations. 46
Figure 4.13: 3D center of keratocytes. 47
Figure 4.14: Schematic representation of the five stromal layers. 48
Figure 4.15: 3D keratocytes centers. 48
Figure 4.16: 3D keratocytes centers in the anterior stroma. 48
Figure 4.17: 3D keratocytes centers in the anterior mid stroma 49
Figure 4.18: 3D keratocytes centers in the central mid stroma 49
Figure 4.19: 3D keratocytes centers in the posterior mid stroma 49
Figure 4.20: 3D keratocytes centers in the posterior stroma 49
Figure 4.21: automatic keratocyte density (mean ± standard deviation) 51
Figure 4.22: 3D object. It is the 3D reconstruction from a sequence of 127 images. 52
Figure 4.23: 2D contour and center of keratocytes, found using the GVF. 53

Figure 5.1: A representative image of cornea endothelium. 55
Figure 5.2: Original image and pre-processed version 56
Figure 5.3: training input image (120x120 pixels) 59
Figure 5.4: training target image (cell bodies and cell boundaries) 59
Figure 5.5: training input image (120x120 pixels) 60
Figure 5.6: ANN output. 60
Figure 5.7: Original image and its entropy. 61
Figure 5.8: Original image and its power spectral density. 62
Figure 5.9: Entropy and PSD liner combination (left) and ROI selection (right). 62
Figure 5.10: Connections of skeleton floating stumps. 63
Figure 5.11: Selected ROI and segmented image after contour completion. 64
Figure 5.12: Merge cells 64
Figure 5.13: Split cells (method 1). 65
Figure 5.14: Split cells (method 2). 65
Figure 5.15: Automatic cell contour detection. 66
Figure 5.16: Scatter-plot of cell density from manual vs. automatic method. 68
Figure 5.17: Bland-Altman plot for cell density. 68
Figure 5.18: Scatter-plot of pleomorphism from manual vs. automatic method. 68
Figure 5.19: Bland-Altman plot for pleomorphism. 68
Figure 5.20: Scatter-plot of polymegathism from manual vs. automatic method. 69
Figure 5.21: Bland-Altman plot for polymegathism. 69

List of Table:

Table 3.1: Statistics of detected lengths of nerve structures in the images of dataset nr.1, for whole images or ROIs and using the manual or automatic method. 29
Table 3.2: Statistics of detected density of nerve structures in the images of dataset nr.1, for whole images or ROIs and using the manual or automatic method. 30
Table 3.3: Statistics of percent of correctly detected lengths of nerve structures (with respect to manually detected nerves) and of false detection (with respect to total automatically detected nerves) in the dataset images, for whole images or ROIs. 30

Table 4.1: automatic keratocyte density 50
Table 4.2: manual keratocyte density. 50
Table 4.3: Percent differences between automatic keratocyte density and the corresponding manual one. 50
Table 4.4: automatic keratocyte density (mean ± standard deviation) 51

Table 5.1: Results obtained using a dataset of 27 images. 65
Table 5.2: Statistics of estimated density in the 27 images. 66
Table 5.3: Statistics of estimated pleomorphism (percentage of hexagonal cells) in the 27 images. 67
Table 5.4: Statistics of estimated polymegathism (standard deviation / average of cell areas) in the 27 images. 67

Sommario

Questa tesi tratta dell’analisi automatica di immagini confocali della cornea, e della stima automatica di parametri clinici.

Malattie e distrofie della cornea (sindrome dell’occhio secco, cheratocono, congiuntiviti, cheratite erpetica, distrofia reticolare, ecc) pregiudicano la visione in molti modi. Alcune causano grave disabilità visiva, mentre poche altre non causano problemi di vista e sono scoperte nel corso di un esame degli occhi. Altre distrofie posso causare ripetuti episodi di dolore senza provocare la perdita permanente della vista. Le strutture della cornea sono molto sensibili alle patologie corneali: le fibre nervose, i cheratociti, le cellule endoteliali modificano la loro morfologia. Cambiamenti nella morfologia delle strutture della cornea sono anche legati all'età o all’uso prolungato di lenti a contatto, ad interventi chirurgici della cornea, come LASIK o PRK, o al trapianto.

La microscopia confocale della cornea permette di acquisire in vivo, in modo rapido e non invasivo, immagini dei vari strati della cornea e delle sue strutture. Analizzare queste immagini ha dimostrato essere molto importante per fornire informazioni cliniche sullo stato di salute della cornea. Allo stato attuale, tutte le analisi delle strutture corneali sono basate su metodi manuali o semi-automatici, e quindi i valori dei parametri clinici che ne derivano sono soggettivi e inclini all’errore.

Per questi motivi, un affidabile strumento automatico per la valutazione delle patologie della cornea è fortemente raccomandato. Ogni metodo automatico per analizzare la cornea deve passare attraverso alcune fasi ben definite. In primo luogo, deve riuscire ad individuare le principali strutture anatomiche della cornea: fibre nervose, cheratociti e cellule endoteliali. Poi, deve misurare quantitativamente le strutture individuate. Infine, deve stimare i parametri di interesse clinico.

In questa tesi, un nuovo algoritmo per estrarre le fibre nervose verrà descritto. Densità e morfologia dei nervi sono correlate a patologie della cornea. Successivamente, sarà presentato un metodo per la visualizzazione di tutte le strutture della cornea nel volume 3D. La densità volumetrica dei cheratociti è un

importante parametro clinico: un algoritmo per il riconoscimento automatico dei cheratociti nel volume 3D e per la stima della densità volumetrica è stato sviluppato. Infine, un algoritmo per il riconoscimento automatico dei bordi delle cellule endoteliali e la stima della densità e morfologia cellulare sarà descritto.

Gli algoritmi presentati in questa tesi rendono possibile pensare ad uno strumento da utilizzare per l'analisi automatica della cornea. Consentirà di ottenere una stima quantitativa e una descrizione riproducibile di tutta la cornea e dettagli quantitativi delle singole strutture. Potrà essere uno strumento diagnostico di aiuto alla pratica clinica.

Summary

This thesis deals with the automatic analysis of confocal images of the cornea, and with the automatic estimation of clinical parameters.

Corneal diseases and dystrophies (dry-eye, keratoconus, conjunctivitis, herpes keratitis, lattice dystrophy, etc.) affect vision in widely differing ways. Some cause severe visual impairment, while a few cause no vision problems and are discovered during an eye examination. Other dystrophies may cause repeated episodes of pain without leading to permanent loss of vision. Corneal structures are very sensitive to corneal pathologies: nerve fibers, keratocytes, endothelial cells change their morphology. Changes in the morphology of corneal structures are also related to age or prolonged contact lens wear, to surgical interventions on cornea, such as LASIK or PRK, or to transplantation.

In vivo confocal microscopy of the cornea allows to acquire in a rapid and non-invasive way images of the various corneal layers and structures. Analyzing these images has been shown to be quite important to provide clinical information on the cornea state of health. At present, all the analyses of corneal structures are based on manual or semi-automatic methods, and thus the derived clinical parameter values are subjective and error prone.

Thus, a reliable automatic tool for evaluating corneal pathologies is strongly needed. Every automatic method for analyzing the cornea must go through some well defined steps. First, it has to detect the main anatomical structures of the cornea: nerve fibers, keratocytes and endothelial cells. Then it has to quantitatively measure the identified structures. Finally, it has to estimate the parameters of clinical interest.

In this thesis a new algorithm to extract the nerve fibers will be described. Density and morphology of nerve fibers are correlated to corneal pathologies. Then a method for visualizing all corneal structures in the 3D volume will be presented. Keratocytes volumetric density is an important clinical parameter: an algorithm for the automatic recognition of keratocytes in the 3D volume and for the estimation of the volumetric density has been developed. Finally, an algorithm for the automatic endothelial cell

contour detection and the estimation of cells density and morphology will be described.

The algorithms presented in this thesis make it possible to conceive a tool to be used for the automatic analyses of the cornea. It will allow to obtain a quantitative and reproducible description of the whole cornea and specific details of the individual structures. It shall provide a diagnostic tool to aid the clinical practice.

Chapter 1

Introduction

1.1 Aim and Objectives

The cornea is the external, transparent layer of the eye. It is approximately 500 μm thick, with three main layers and two thin membranes in between [1]: the epithelium on the external side, separated by the Bowman membrane from the thick, central stroma layer, followed by the Descemet membrane and finally the innermost endothelium layer. Changes in the morphology of corneal structures are related to corneal diseases and disorders, to age or prolonged contact lens wear, to surgical interventions on cornea, such as LASIK or PRK, or to transplantation.

In vivo confocal microscopy of the cornea [2] allows to acquire in a rapid and non-invasive way images of the various corneal layers. The following figures show images of corneal layers, they were acquired with a confocal microscope (Confoscan4; Nidek Technologies, Padova, Italy) and cover a field of 460x350 μm.

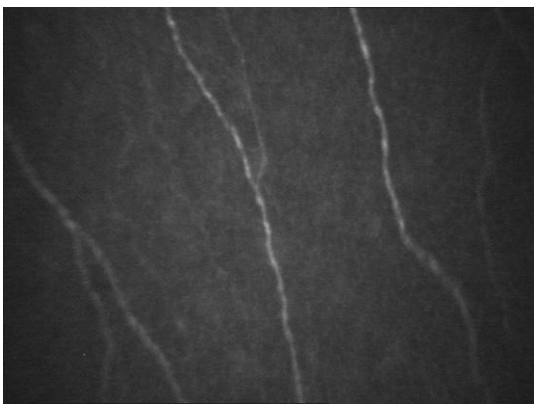

Figure 1.1: Epithelium layer (containing the nerve fibers).

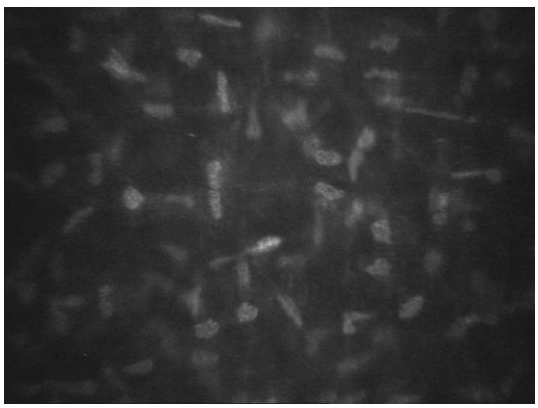

Figure 1.2: Stroma layer (containing the round-shaped keratocytes cells).

Analyzing these images is quite important in order to provide clinical information on the cornea health state. At present, the analyses of corneal structures are based on manual or semi-automatic methods, and thus the derived clinical parameter values are subjective and often error prone. Thus, a reliable automatic tool for evaluating corneal pathologies is strongly needed.

The aim of the work presented in this thesis is to develop a set of tools for the fully automatic analysis of confocal images of the cornea.

In particular, the images collected at a specific depth, the sub-basal layer, allow the visualization of the nerve structures present in this section of the cornea. They are narrow and elongated structures lying flat inside a thin 10 μm layer. These structures have been shown to be quite important to provide clinical information related to changes from age [3] or prolonged contact lens wear [4], from surgical interventions on cornea, such as LASIK or PRK [5, 6] or transplantation [7], or in such pathologies as dry eyes / Sjögren's syndrome [8, 9], keratoconus [10, 11], or herpes keratitis [12]. An important link has been shown between nerve tortuosity and the severity of diabetic neuropathy, one the most common and serious long term complications of diabetes [13]. At present, all these analyses are based on a tedious manual tracing of the nerves and thus the derived clinical parameter values are subjective and error prone. An automatic tool, capable of reliably extracting the nerve course and layout and to quantitatively measure e.g. their density or tortuosity, would provide a much easier, objective and clinically usable procedure.

Analyzing corneal structures, e.g. nerves or keratocytes, in the whole volume of the cornea and not only in a layer at a specific depth has been shown to be quite important [14, 15]. For example, nerves fibers are mainly located in the sub-basal layer (a specific surface inside epithelium), but they also penetrate the Bowman membrane, epithelium and stroma running orthogonally [16]. Keratocytes are present in the full thickness of stroma, their nuclei are visible as bright objects (the cell bodies are larger and usually not visible) against the dark background of the extracellular tissue, and their density is an important clinical parameter. Keratocytes are fibroblast-like cells that maintain the health and clarity of the corneal stroma. Several investigators have examined changes in density of these cells with age [17], with contact lens wear [18], keratoconus [19], after refractive surgery [20, 21], and after corneal transplantation [22]. The accuracy and precision of manually counting cell nuclei depends on the ability of the observer to discriminate nuclei from the background noise in the image and to interpret the variable appearance of cell nuclei located at different depths within the optical section of the image. Nuclei with the highest contrast and sharpest edges can be consistently identified, whereas those with lower contrast and blurred edges will be inconsistently identified. Because of this subjectivity, two investigators, or one investigator assessing density in the same images on two sessions, rarely arrive at exactly the same density [23, 55]. Currently this density is calculated on the 2D images, but stroma represents, on average, 80% to 90% of the whole corneal volume and it is important to analyze the 3D arrangement and density of stromal keratocytes [24]. A program that identifies and selects cells in confocal images would be more objective than manual assessment of low contrast images. The purpose is to provide a three-dimensional reconstruction (starting from a sequence of 2D images) that allows visualization and analysis of all corneal structures in the 3D volume, and the automatic estimation of the keratocytes volumetric density.

The analysis of microscopy images of corneal endothelium is also quite important to assess cornea health state and quality. Clinicians are interested in determining cell

density and cell morphology [25, 26, 27], since these features can be used as early indicators of corneal pathologies or in the typing of corneas for possible transplants. Endothelial cells are polygonal with four to eight borders, mostly hexagonal. They have a diameter of about 22 μm and a surface area of about 250 μm^2. Ideal endothelia are made of regular hexagonal cells of similar area, but this regular tessellation is affected by age and pathologies. Corneal endothelial cells do not reproduce, therefore pathologies affecting the endothelium permanently damage the layer. Death of corneal endothelial cells is compensated by enlargement and migration of neighboring cells, which change the regular hexagonal pattern. The deviation of the cell field from the regular hexagonal pattern is therefore an indicator of the corneal damage. A quantitative analysis may provide information on cell density, polymegathism (distribution of cell sizes), and pleomorphism (distribution of number of cell sides). The availability of an automatic system for image processing would be an immense aid.

1.2 Outline of the thesis

Chapter 2 is an introductory chapter describing the eye anatomy, the cornea morphology and all its layers and structures. Confocal microscopy principles and exams are also described.

The extraction of the nerve structures is the object of the chapter 3.

Chapter 4 contains the 3D reconstruction and visualization of all corneal structures in the 3D volume, and the automatic recognition of keratocytes, with the estimation of their volumetric density.

In chapter 5, an automatic analysis of corneal endothelium based on the identification of cell contours is proposed

A brief discussion, summarizing the results presented in each chapter, with lines for further development is contained in Chapter 6.

Chapter 2

The Cornea

2.1 Eye anatomy

The eye is a complex organ composed of many parts. Good vision depends on the way in which those parts work together. Vision is the most used of the 5 senses and is one of the primary means that we use to gather information from our surroundings. The eye has a spherical shape, dimensions vary only 1–2 mm among humans. The vertical diameter is 24 mm, the transverse being larger. Light comes through the cornea and the amount of light coming in is controlled by the pupil, and it is focused on the retina. The retina reacts to the incoming light and sends a record of it via the optic nerve to the brain.

As light enters the eye, it passes through (Figure 2.1):

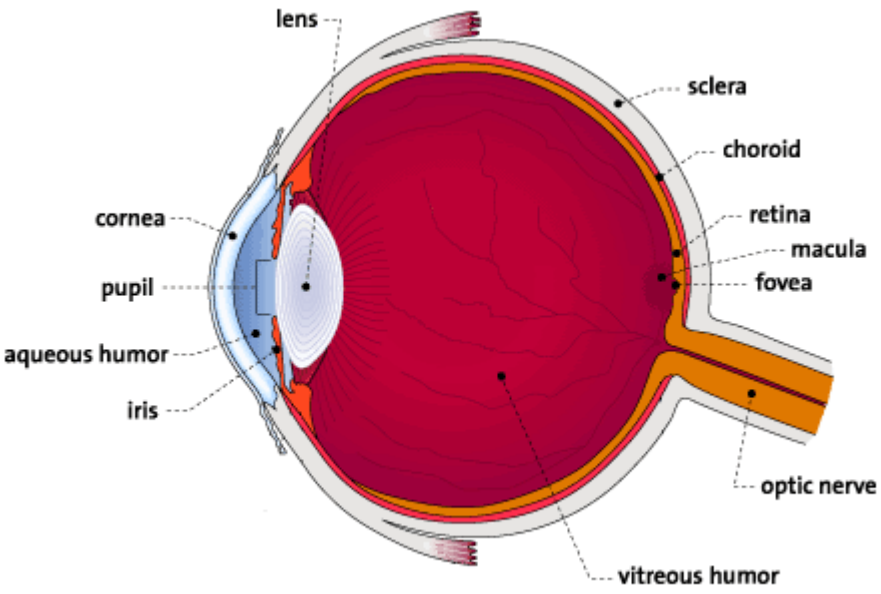

Figure 2.1: Eye Anatomy.

- *the cornea*
  It is the clear part of the eye, covering the iris and the pupil. The main purpose of the cornea is to help focus light as it enters the eye.

- *the aqueous humor*
  It is a clear fluid in the front of the eye, between the cornea and the iris, that provides nutrients to the cornea and the lens. It maintains a constant pressure inside the eye. The fluid is produced by the ciliary body.

- *the iris*
  It is a complex tissue that lies between the cornea and the lens. It is the colored part of the eye. The iris may dilate to make the pupil bigger or constrict to make the pupil smaller, thereby controlling the amount of light that enters the eye.

- *the pupil*
  It is the round, dark center of the eye, which opens and closes to regulate the amount of light that enters the eye.

- *the lens*
  It is the nearly spherical body in the eye, located behind the cornea. The lens can change its shape to modify its optical power so a clear image of objects at various distances can be focused on the retina.

- *the vitreous humor*
  After being focused by the lens, light passes through the center of the eye, which is fill with the vitreous humor. It is a clear, jelly-like fluid. The vitreous fills the entire globe, from the lens to the retina, it helps maintain the shape of the eye.

- *the retina*
  It is a thin, light-sensitive tissue lining the back of the eye that acts much like film in a camera. It receives images formed by the lens and converts them into signals that reach the brain by way of the optic nerve. The retina is a complex, layered structure with several layers of neurons interconnected by synapses. The only neurons that are directly sensitive to light are the photoreceptor cells. These are mainly of two types: rods and cones. Rods are more sensitive to light; therefore, they allow to see in low light situations but do not allow to see color. Cones, on the other hand, allows to see color but require more light. The retinal blood vessels nourish the inner layers of the retina.

- *the macula*
  It is on the visual axis. Within the macula are the fovea, which contain a high density of cones. They provide a means of high acuity vision because of the high density of receptor cells.

- *the fovea*
  It is a depression in the center of the macula region of the retina that contains only cones (not rods).

- *the choroid*
  It consists of layers of blood vessels located between the sclera and the retina. They supplies oxygen and nutrients to the outer layers of the retina.

- *the sclera*
  It is the white part of the eye. The sclera is composed of tough, fibrous tissue, also extended around the eye. It protects the eye and gives the eye its shape.

- *the optic nerve*
  It is a bundle of nerves fibers, it is responsible for transmitting nerve signals from the eye to the brain. These nerve signals contain information on an image for processing by the brain. The front surface of the optic nerve, which is visible on the retina, is called the optic disk.

2.2 Corneal morphology

The cornea (Figure 2.2) is the transparent front part of the eye that covers the iris, pupil, and anterior chamber. Together with the lens, the cornea refracts light, and as a result helps the eye to focus, accounting for approximately 80% of the eye's optical power. The cornea has nerve endings sensitive to touch, temperature and chemicals; a touch of the cornea causes an involuntary reflex to close the eyelid. Because transparency is of prime importance the cornea does not have blood vessels; it receives nutrients via diffusion from the tear fluid at the outside and the aqueous humor at the inside and also from proteins supplied by nerve fibers that innervate it. In humans, the cornea has a diameter of about 11.5 mm and a thickness of 0.5–0.6 mm in the center and 0.6–0.8 mm at the periphery. Transparency, avascularity, and immunologic privilege makes the cornea a very special tissue. The cornea is the only part of a human body that has no blood supply; it gets oxygen directly through the air. It borders with the sclera by the corneal limbus.

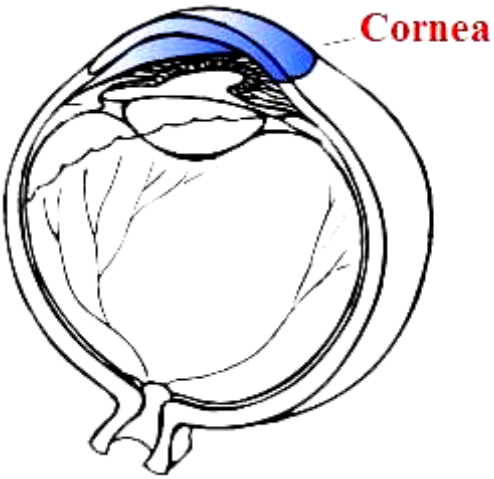

Figure 2.2: The Cornea.

The cornea has three main layers, with two thin membranes in between [1]. From the anterior to posterior they are (Figure 2.3):

- Epithelium;
- Bowman's membrane;
- Stroma;
- Descemet's membrane;
- Endothelium;

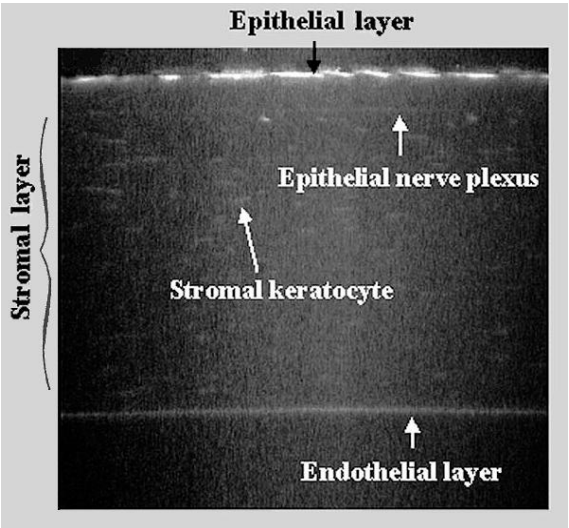

Figure 2.3: Reconstruction of corneal layers.

The epithelium covers the surface of the cornea. The average thickness of the whole epithelium is approximately 50 μm, about 10 percent of the cornea's thickness. The epithelium functions primarily to block the passage of foreign material, such as dust or water, into the eye and other layers of the cornea, and provide a smooth surface that absorbs oxygen and other needed cell nutrients that are contained in tears. It is composed of five to six cellular layers and quickly regenerates when the cornea is injured. Superficial epithelial cells appear polygonal in shape, generally with evident nuclei, well-defined cellular borders, and homogeneous in density. Basal epithelial cells instead appear as smaller polygonal cells, thus presenting a higher density, without evident nuclei and with very well-defined and bright cellular edges. Intermediate cells present borderline characteristics. This layer is filled with thousands of tiny nerve endings that make the cornea extremely sensitive to pain when rubbed or scratched.

Bowman's membrane lies just beneath the epithelium It is a tough layer that protects the corneal stroma, consisting of irregularly-arranged collagen fibers. It is 8 to 14 μm thick.

Stroma represents, on average, 90% of the whole corneal volume. Within its structure, it is possible to recognize cellular, acellular and neurosensory components. The cellular components is mainly composed of keratocytes which represent approximately 5% of the entire volume. The acellular part includes regular collagen lamellar structures and interstitial substance. The last part is represented by the stromal nerve plexus together with isolated stromal nerves fibers. The mean density of keratocytes is higher in the anterior stroma and it decreases while moving towards the posterior stroma.

The Descemet's membrane lies between the stroma and the endothelium. It is a thin acellular layer that serves as the modified basement membrane of the corneal endothelium.

The endothelium is the most posterior layer of the cornea and it is formed by a single layer of cells which derived from the neural crest. Descemet's membrane and endothelium are not innervated. In childhood, endothelial cells presents uniform hexagonal shape and homogeneous size, with a density that is generally higher in comparison with the one in older subjects. During life, a percentage of endothelial cells may assume different polygonal shapes as the cell density decrease.

The following figures show images of corneal layers, they were acquired with a confocal microscope (Confoscan4; Nidek Technologies, Padova, Italy), and cover a field of 460x350 μm.

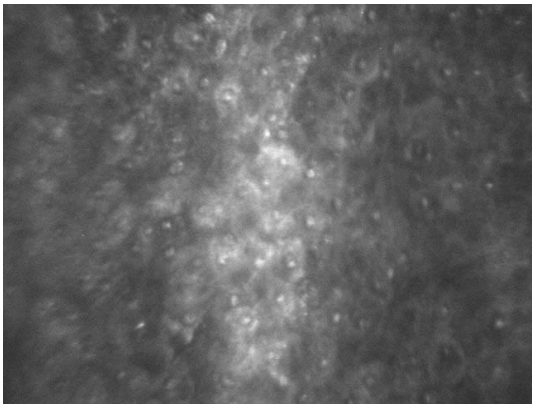

Figure 2.4: Superficial epithelium.

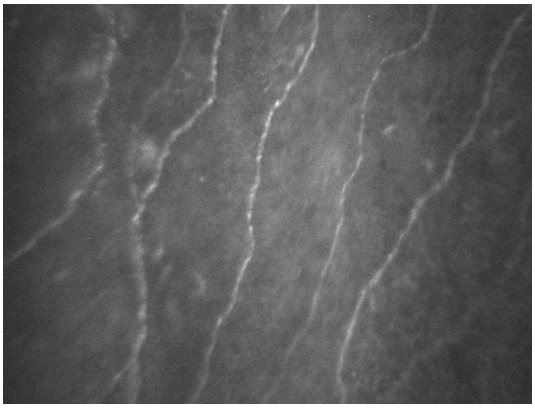

Figure 2.5: Sub-epithelial nerve plexus.

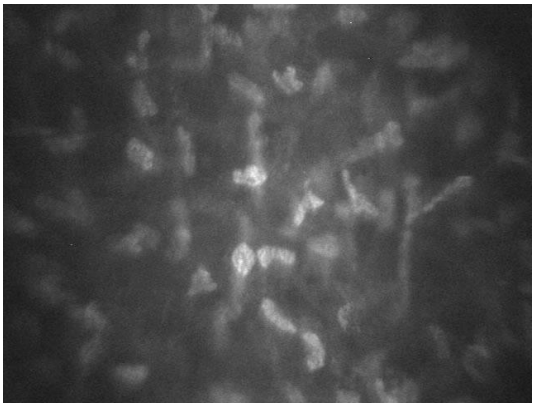

Figure 2.6: Stroma.

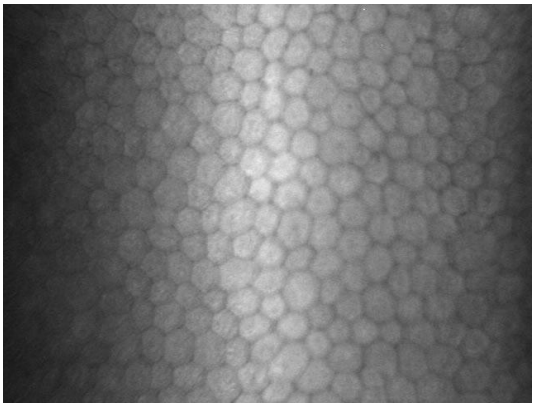

Figure 2.7: Endothelium.

2.3 Corneal innervations

The cornea is one of the most sensitive tissues of the body, it is densely innervated with sensory nerve fibers. Confocal microscopy gives the opportunity to study the morphology of corneal innervations (Figure 2.8).

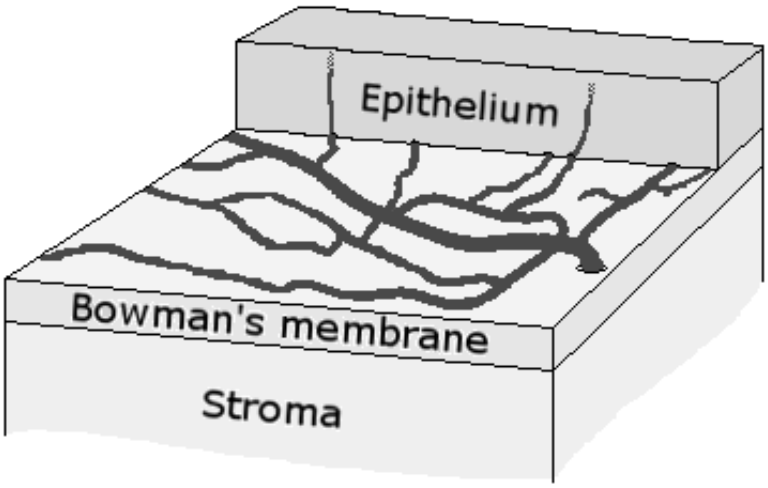

Figure 2.8: Corneal innervations.

Sub-basal nerve plexus, which runs between the basal cellular layer and the most anterior part of the Bowman's membrane, and the sub-epithelial nerve plexus, which is located below the Bowman's membrane, are clearly visible in healthy corneas. Corneal nerves derived from the long ciliary nerves which come from the ophthalmic branch of the trigeminus. At the level of sclerocorneal limbus, the nerve fibers derived from the long ciliary nerves are arranged into a circular plexus from which originate other fibers. These fibers run radially with several anastomosis within the rear stroma, forming the deep corneal plexus. Thin vertical fibers originate from this plexus and they form the sub-epihelial nerve plexus. Perforating the Bowman's membrane at the level of the basal epithelium, they form the sub-basal nerve plexus. Its fibers run superficially, providing innervations to the basal epithelium cell layer and terminating within the superficial epithelial layers. The stromal nerve plexus, instead, are located in the anterior-mid and mid stroma. In the stroma, nerve fibers are thin bright and reflective nerve fibers, disposed into vertical or oblique parallel orientation with several bifurcations. The thickness of single sub-basal nerve fibers usually ranges from 2 to 4 μm, while the sub-epithelial fibers are on average 3 to 7 μm in width. Stromal fibers ranges from 4 to 14 μm.

2.4 Confocal microscopy

Confocal microscopy is a technique for obtaining high-resolution optical images. The key feature of confocal microscopy is its ability to produce in-focus images of thick specimens, a process known as optical sectioning. Images are acquired point-by-point and reconstructed with a computer. The principle of confocal microscopy was originally patented by Marvin Minsky in 1957. In vivo confocal imaging of the

cornea has evolved exponentially over the last few decades and it has increasingly emerged from the laboratory to be used in the clinical setting in relation to inherited corneal diseases, corneal infections, contact lens wear and the effects of corneal surgery. This evolution has led to significant enhancement of our knowledge of the living cornea in both its physiological and pathological states. In the recent years, many researchers investigated the cornea using confocal microscopy. This tool is useful to acquire in a rapid, in vivo and noninvasive way images from all corneal layers and membranes.

Figure 2.9: Confocal microscope exam.

The central region of the cornea is examined using a coupling medium (gel) between eye and front surface of the lens (Figure 2.9). The front surface of the lens is advanced with a joystick attached to the main body of the instrument until the anterior layers of the cornea are visualized and then image acquisition begins when the objective lens is properly positioned on the corneal apex by the instrument auto-alignment module. The light is projected onto the cornea and passes through one half of the front lens (Figure 2.10). Most of the light is concentrated inside the focal point. In order to minimize the scattering light, just a small area inside the cornea is illuminated. A small illuminated slit is projected into the cornea, similar to a slit lamp. The small amount of the reflected light passes through the other half of the front lens and a second slit, with the same size of the optical setup of the illumination slit. Finally, this image is projected onto a highly sensitive camera and displayed on the monitor. Due to this optical arrangement, all the unwanted light coming from the unfocused layers is cut off by the second slit: only the slit image is conjugated to the slit opening. In order to see a large area, the slits are in motion and scan the cornea. Lateral motion of the vertical slits provide a lateral scan to create the image. The confocal microscope records a sequence of a patient's cornea images starting from the anterior chamber, and then it moves the optical head back and forth through the cornea layers. The movement of the front lens (with interposition of transparent gel) backward and forward permits scanning of the entire cornea. Images of few μm of thickness and 460 x 350 μm in width are acquired during the scan. Each image is associated with an axial position (z). The distance between each image is variable according to the parameters set for the acquisition, it is typically 2 to 8 μm. An important feature of confocal microscopes is the depth of field: keeping it small (few μm) makes these instruments very useful for anatomical studies of the cornea. A thin depth of field permits a better quality of image and a correct positioning of all corneal structures along z direction. In order to increase image stability and to have a precise location along z-axis, images can be acquired using the "Z-Ring system", a positional sensor that is in contact with the eye.

The confocal microscope is able to show separate layers of transparent organic structures and tissue of the human cornea in high magnification. On average, total duration of the examination is 2 minutes, and image acquisition time is 30 to 60 seconds.

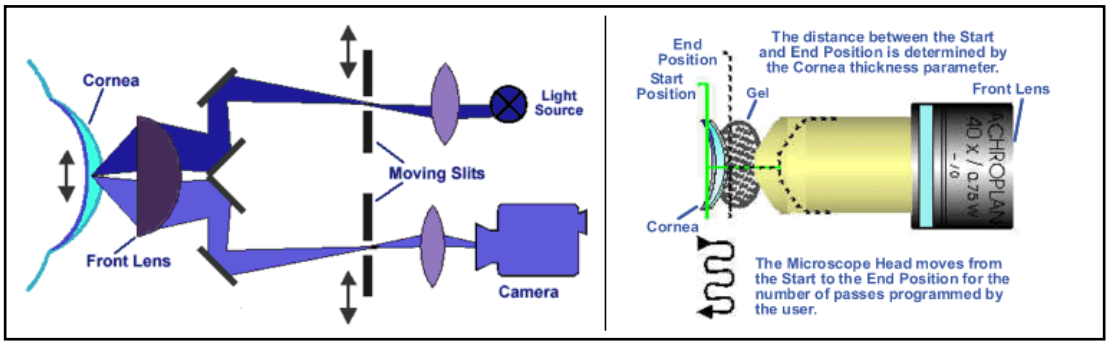

Figure 2.10: Confocal microscope arrangement.

Chapter 3

Nerves Tracing

3.1 Materials

The images collected at a specific depth, the sub-basal layer, allow the visualization of the nerve structures present in this section of the cornea (Figure 3.10). They are narrow and elongated structures lying flat inside a thin 10 μm layer.

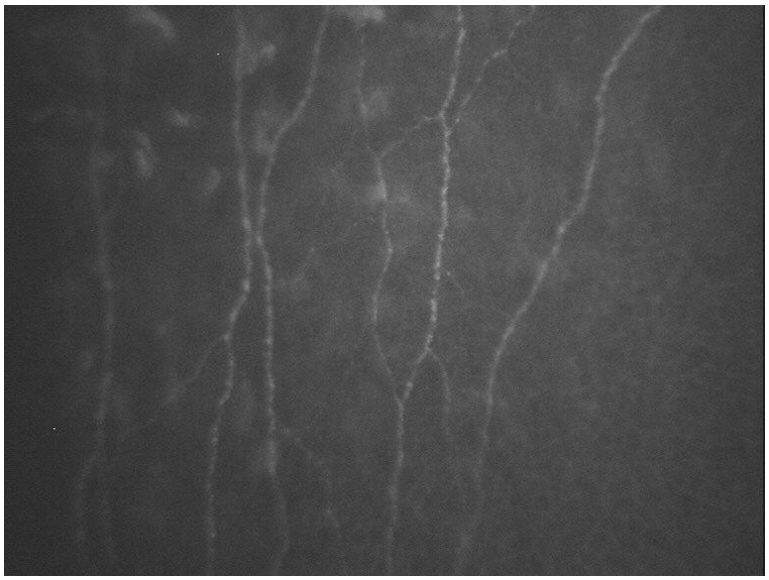

Figure 3.1: A representative image of corneal sub-basal layer obtained with the Confoscan4 confocal microscope (Nidek Technologies; Italy).

These structures have been shown to be quite important to provide clinical information related to changes from age [3] or prolonged contact lens wear [4]; from surgical interventions on cornea, such as LASIK or PRK [5, 6] or transplantation [7], or in such pathologies as dry eyes / Sjögren's syndrome [8, 9], keratoconus [10, 11],

or herpes keratitis [12]. An important link has been shown between nerve tortuosity and the severity of diabetic neuropathy, one the most common and serious long term complications of diabetes [13]. At present, all these analyses are based on a tedious manual tracing of the nerves and thus the derived clinical parameter values are subjective and error prone. An automatic tool, capable of reliably extracting the nerve course and layout and to quantitatively measure e.g. their density or tortuosity, would provide a much easier, objective and clinically usable procedure.

Images of corneal sub-basal epithelium were acquired with the ConfoScan 4 confocal microscope (Nidek Technologies, Italy). These images cover a field of 460x350 μm, they were acquired at 40X magnification and saved as monochrome 768x576 pixel digital images.

Recognizing corneal nerves has some similarities with the vessel tracking task in retinal images. For this reason, the approach has been to start with an algorithm developed for the latter task [28] and then to modify it, also with the addition of new modules specifically aimed at the analysis of images of corneal sub-basal epithelium.

3.2 Luminosity and contrast normalization

Acquired images do not usually have a uniform luminosity and contrast, exhibiting e.g. darker areas in the peripheral regions of the image. This is due to many factors, including the spherical shape of corneal layers, which causes a non uniform reflection of illumination light in the different corneal areas, and the different attenuation of light along the various illumination paths. In order to compensate for this, a specific equalization procedure, which was originally developed to normalize luminosity and contrast in retinal images [29], was applied. The method is based on a
model of the observed image I:

$$I = f(I^0) = f(I_b^0 + I_f^0)$$

where I^0 is the original image, I_b^0 is the (original) background image, I_f^0 is the (original) foreground image, and function $f(.)$ represents the acquisition transformation. The background image I_b^0 is the ideal image of a corneal sub-basal layer free of any corneal structure. The corneal structures are modeled as an additive term I_f^0 to the background image. The acquisition model $f(.)$ describes the contrast and luminosity distortions introduced by the image observation process. Non-uniform contrast and luminosity within an image can be described as:

$$I(x,y) = f(I^0(x,y)) = C(x,y)I^0(x,y) + L(x,y)$$

where $C(x,y)$ is the contrast drift factor and $L(x,y)$ is the luminosity drift term. Both contrast and luminosity drifts are space-dependent scalar functions and can therefore be considered as images themselves. The recovery of an estimate $\hat{I}^0$ of original image I^0 is based on the estimation of C and L ($\hat{C}$ and $\hat{L}$), and the compensation of the observed image I as:

$$\dot{I}^{0}(x,y) = \frac{I(x,y) - L^{\wedge}(x,y)}{C^{\wedge}(x,y)}$$

The proposed method derives estimates $L^{\wedge}$ and $C^{\wedge}$ from the background component of the observed image $I(x,y)$ by estimating mean and standard deviation [30]. Luminosity and contrast variability estimated in the background part of the image are then used for the normalization of the whole image. As this procedure increases the amplitude of noise as well, a median filter is then applied to reduce this artifact. In pre-processed images, nerve structures have a higher contrast with respect to background and appear more visible, even in the peripheral areas of the image (Figure 3.2).

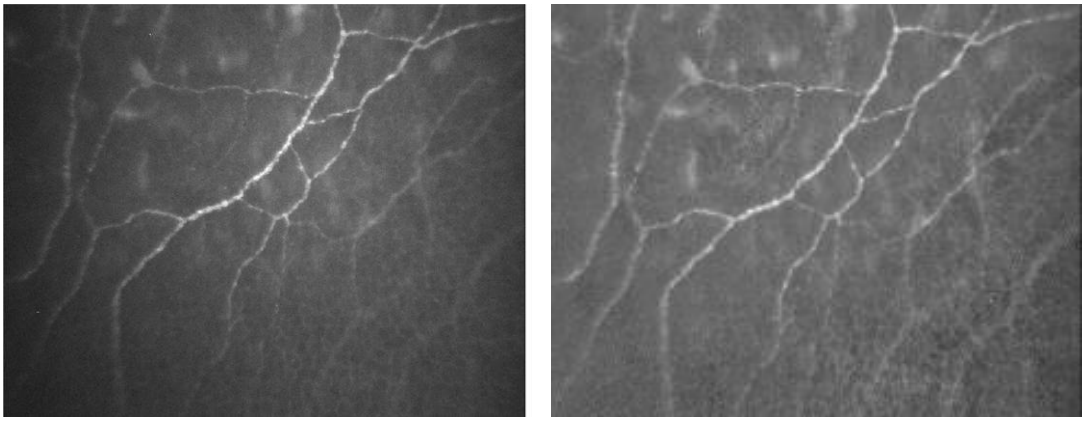

Figure 3.2: Original image and pre-processed normalized version.

3.3 Seed points extraction

The algorithm starts by identifying a set of seed points, to be used as starting points for a nerve tracking procedure. A line grid of equally-spaced rows and columns (one every 10 pixels) is drawn over the image and its pixels are analyzed by looking for variations in their gray level intensity that may suggest an intersection with nerves. A detection threshold was empirically set at 0.8 times the average gray level over the whole image and all analyzed pixels exceeding this threshold were considered as seeds, i.e. pixels belonging to nerves. A sequence of consecutive "nerve" pixels is interpreted as a nerve profile, and the seed point is set in the center of the nerve profile. In order to reduce the total number of detected seed points, nerves with very large caliber (possible artifacts) or very small (negligible nerves) are searched and removed. Moreover, if a local intensity variability σ_N is defined as the standard deviation of pixel intensities in a 40x40 neighborhood around a seed point, seed points positioned on a nerve will have high values of σ_N , due to the presence in the neighborhood of both "nerve" (light) and "non-nerve" (dark) pixels. Mean μ and standard deviation σ of the σ_N of all the seed points are computed and seed points with a low value of the local intensity variability, e.g. lower than μ-$k\sigma$, are also removed; k is a constant empirically determined. To further reduce the number of seed points, a clustering procedure is performed. It starts by clustering the

two closest seed points whose distance is lower than a threshold δ and then proceeds by iteratively adding to the cluster all the seed points that have distances from all the seed points in the cluster lower than δ. This iterative addition ends when no new seed points match the clustering condition. The whole procedure is iterated until all seed points have been examined and clustered. The seed points with the highest intensity value (lightest) in each cluster are taken as the representatives of the cluster and are the ones returned by the clustering algorithm.

On average, 600 seed points per image are detected. Lower values of the threshold, which actually provide more seed points, do not however yielded overall better tracing results.

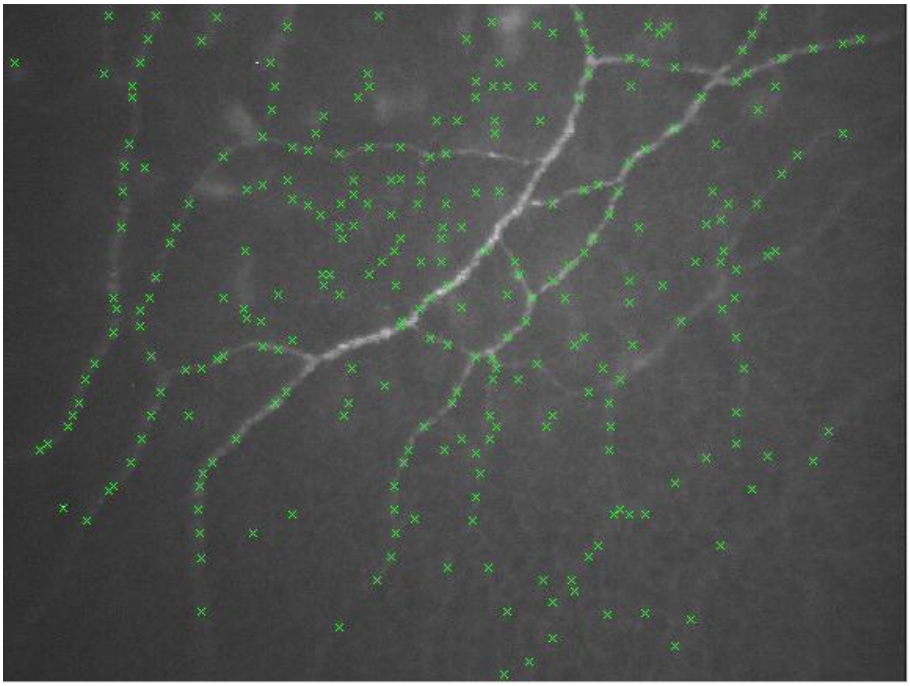

Figure 3.3: Seed points extraction.

3.4 Bubble analysis

Seeds points extracted have no information on the direction and caliber of their correspondent nerve. Before the tracking procedure can start, an initial estimate of this nerve direction has to be extracted. This is done by means of a "bubble analysis" technique, which will be further used to find possible nerve paths in critical situations, i.e. when the tracking is not able to move further along a nerve due to presence of bifurcations or crossings or to poor image contrast. The idea of the "bubble analysis" is to look in concentric circular lines around a point, in an attempt to look "beyond" local information or critical points.

The *Bubble Analysis* procedure consists of the following steps:

1. concentric circular scan lines are analyzed around the point;

2. nerve profiles are extracted along these scan lines and nerve centers and calibers are determined;

3. center points are filtered by the Hough transform to eliminate spurious recognitions;

4. center points are transformed into polar space and clustered;

5. cluster centers are added to set of seed points.

In the first two steps of the procedure, pixels of each circular line are clustered with a fuzzy c-mean algorithm [31], using their gray-level values as classification feature. The fuzzy c-mean algorithm assigns to each pixel a degree of membership to a class, in this way a fuzzy set is created. After defuzzification (the process of producing a quantifiable result from a fuzzy set), a two-class separation is obtained for the pixels along every circular line: the "nerve" and "non-nerve" classes. It can be assumed that in the small neighborhood around the end-point covered by bubbles, nerves that may be present can be considered as straight lines moving radially away from the end-point. This means that the center points of each nerve are aligned along a straight line. In order to remove spurious nerve center recognitions, the whole set of center points is filtered by the Hough transform. In the Hough transform space, each point is represented by a sinusoid, and all the points aligned along a straight line have sinusoids with a common intersection. Therefore, spurious center points are represented by sinusoids that do not pass through these common intersections and can thus be recognized and removed (Figure 3.4).

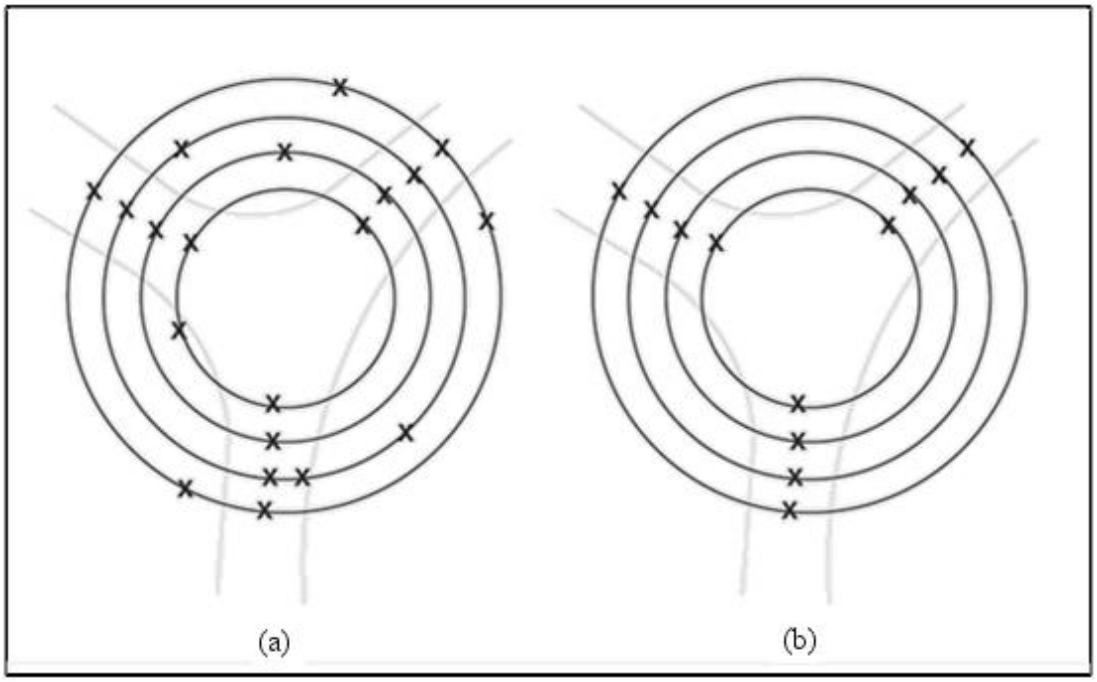

Figure 3.4: Seed points before (a) and after (b) Hough transform.

The remaining points are then transformed into a polar coordinates space, having the seed point as its origin. Under the assumption made above, the polar representation

allows a much better Euclidean separation of the points into clusters than the Cartesian representation. A two-dimension fuzzy c-mean technique is used for clustering, and the resulting clusters of center points identifies the nerve segments that are present in the neighborhood. Further fixing of these clusters is performed by merging close clusters and removing very small clusters. An initial caliber is estimated as the average of the calibers of the points belonging to the cluster, while an initial nerve direction is extracted by a Principal Components Analysis (it is a vector space transform widely used in data analysis and compression) on the same set of points. In case of one nerve present around the center of the circular lines, only one direction will be found, and this will be the initial estimate for the tracking module. If one or more relevant directions are found, the seed point is discarded. However, when looking for new tracking paths beyond a critical point, all relevant directions in the Hough transform are kept: seed points are placed at a suitable distance from the critical point along each identified direction: this ensures the possibility for the tracking algorithm to overcome bifurcations and crossings.

3.5 Tracing

This module is based on a step by step analysis of consecutive linear scan lines *SL*. The position of the scan line in the image determines which image pixels are under analysis. For the scan line SL_i , examined at step *i*, a *scan line analysis* classifies the pixels and identifies all possible nerve profiles VP_i. In general, n_i different nerve profiles may be identified on SL_i, since more than one nerve or a keratocyte or just random noise may be present. Center c_{ij} and caliber d_{ij} of every j^{th} ($j = 1 \ldots n_i$) nerve profile vp_{ij} are determined.
Among all the n_i nerve profiles vp_{ij} detected on SL_i, a *nerve profile selection* function *P* selects vp_i, the sole profile to be associated with SL_i, i.e., the one belonging to the nerve being tracked, using information on centers and calibers detected on the previous scan line SL_{i-1}: $vp_i = P\ (VP_i,\ c_{i-1},\ d_{i-1})$. Scan line updating, i.e., the determination of the new scan line SL_{i+1} given the past history, is determined by a *scan line updating* function *U*, which determines the position of SL_{i+1} using information on centers and calibers detected on the previous and current scan lines, $SL_{i+1} = U\ (c_i, c_{i-1}, d_i, d_{i-1})$.

3.5.1 Scan line analysis

The pixel classifier adopted here is based on a Fuzzy C-Means (FCM) clustering Algorithm. The intensity values of the pixels p_k of a generic scan line *SL* are examined and classified into two classes: "nerve" (*v*) and "non-nevre" (~*v*). The classifier returns a vector $\{P_k^v(SL)\}$, which contains the probability of each pixel p_k in *SL* of being "nerve" (the probability of being "non-nerve" can be evaluated by taking the complementary to the previous one, i.e., $P_k^{\sim v}(SL) = 1 - P_k^v(SL)$. The classification of pixel p_k is then done by applying a threshold to its probability $P_k^v(SL)$. The scan line is analyzed to determine all the sequences of consecutive pixels classified as "nerve", leading to a first set of candidate nerve profiles VP_i, which is examined as follows:

- all nerve profiles $vp_{ij} \in VP_i$ that are smaller than δ_0 are deleted from VP_i;
- all nerve profiles $(vp_{ij}, vp_{ik}) \in VP_i$ that are closer than δ_1 are merged into a single profile;
- all nerve profiles with contrast κ lower than threshold δ_2 are deleted from VP_i;

where δ_0, δ_1 and δ_2 are user-selected threshold values and the contrast κ of a generic nerve profile *vp* on *SL* is defined as:

$$\kappa(vp,I) = \frac{\left|\beta^{v}(vp,I) - \beta^{\sim v}(vp,I)\right|}{\max\left[\beta^{v}(vp,I) - \beta^{\sim v}(vp,I)\right]}$$

where

$$\beta^{v}(vp,I) = \frac{\sum_{k=1}^{m} P_k^{v}(SL) I(p_k)}{\sum_{k=1}^{m} P_k^{v}(SL)}$$

$$\beta^{\sim v}(vp,I) = \frac{\sum_{k=1}^{m} P_k^{\sim v}(SL) I(p_k)}{\sum_{k=1}^{m} P_k^{\sim v}(SL)}$$

$I(p_k)$ is the intensity of pixels p_k and m is the number of pixels in *SL*. The resulting set of nerve profiles *VP* will not contain any profile with caliber lower than δ_1 or any pair of profiles separated by gaps smaller than δ_0. The first condition was meant to eliminate isolated or short sequences of noisy pixels classified as "nerve" by the FCM classifier, while the second condition was aimed at eliminating from the recognized profiles the isolated pixels incorrectly classified as "non-nerve". For each recognized nerve profile *vp*, center and caliber are evaluated. Nerve center is defined as:

$$c(vp,I) = \frac{\sum_{k=1}^{m} P_k^{v} p_k}{\sum_{k=1}^{m} P_k^{v}}$$

and nerve caliber as:

$$d(vp,I) = \max_{i,j} \left\| p_i - p_j \right\|$$

Note that center evaluation does reach sub-pixel accuracy, while caliber is limited to pixel-accuracy, even though it considers pixel distances in Euclidean terms and not pixel-step terms.

3.5.2 Nerve profile selection

The correct nerve profile vp_i, one for each scan line SL_i, is provided by the *profile selection* function *P* defined as:

$$vp_i = P(VP_i) = \arg\min_{vp_{ij} \in VP_i} s(vp_{ij})$$

where *s* is a score function evaluated for each of the nerve profiles vp_{ij} ($j = 1 \ldots n_i$) identified on SL_i. The proposed score function is a weighted combination of the absolute changes in caliber and direction with respect to *reference* caliber and direction signals d_i* and θ_i*, which are the 2-elements autoregressive filtered values of the caliber and direction series identified on previous scan lines. Score function *s* is defined as:

$$s(vp_{ij}) = \frac{\theta(vp_{ij}) - \theta^*_{i-1}}{w_\theta} + \frac{d(vp_{ij}) - d^*_{i-1}}{w_d}$$

$$\theta^*_{i-1} = \frac{1}{2}\left[\theta^*_{i-2} + \theta_{i-1}\right]$$

$$d^*_{i-1} = \frac{1}{2}\left[d^*_{i-2} + d_{i-1}\right]$$

where $\theta(vp_{ij})$ ($0 \le \theta(vp_{ij}) < 2\pi$) is the direction defined by connecting the center of the current nerve profile, vp_{ij}, and the one selected on the previous scan line, c_{i-1}; θ_i* is the *reference* direction; θ_{i-1} is the direction defined by the centers of the nerve profiles selected on the $(i - 2)^{th}$ and the $(i - 1)^{th}$ scan lines, i.e., c_{i-2} and c_{i-1}. Likewise, d (vp_{ij}) is the caliber of the current nerve profile; d_i* is the *reference* caliber; d_{i-1} is the caliber of the nerve profile selected on the $(i - 1)^{th}$ scan line. The two parameters w_θ and w_d are used to give more importance in the selection of the correct nerve profile either to constancy of direction (θ) or to caliber regularity (d).
The *reference* values provided by the low-pass filtering have been introduced in order to force some regularity in nerve caliber and direction, preventing sharp variations to affect the subsequent steps in nerve profile detection. A maximum value for the score function has been set and profiles for which this maximum value is exceeded are not considered for the selection. This was done in order to avoid tracking of artifacts when no nerve profile is actually present in the scan line. In this case, the detected nerve profiles might be artifacts, which will differ markedly in terms of direction or caliber from the nerve being tracked and will therefore yield a high value of the score function.

3.5.3 Scan line updating

The new scan line SL_{i+1} i.e., the one obtained moving SL_i one step forward along the nerve, is defined as the set of pixels *p:*

$$\left\{ p \middle| p(y) = c_i + \rho(\cos\theta_i, \sin\theta_i) + \frac{\lambda}{2}(\cos(\theta_i + \pi/2), \sin(\theta_i + \pi/2)), -\lambda_{i+1} \le \lambda \le \lambda_{i+1} \right\}$$

where ρ is the *tracking step*, i.e., the distance between SL_i and SL_{i+1}, and λ_{i+1} is the new *scan line size*. Scan line size λ_{i+1} is dynamically set to twice the present *reference* caliber: $\lambda_{i+1} = 2d_i$*, so that it can adapt to the dynamic variation of the nerve caliber size (Figure 3.5). This allows to always have scan lines containing both "nerve" and "non-nerve" pixels and to avoid to examine too many "non-nerve" pixels when the nerve caliber decreases. The tracking step ρ is kept constant until the tracking algorithm reaches a termination point, i.e., when the profile selection function is not able to identify any profile. At this point, in order to overcome a stop that might be caused only by small local artifacts, the tracking step is iteratively decreased by 10% steps, until either tracking is restarted or the maximum number of attempts is reached and tracking ends.

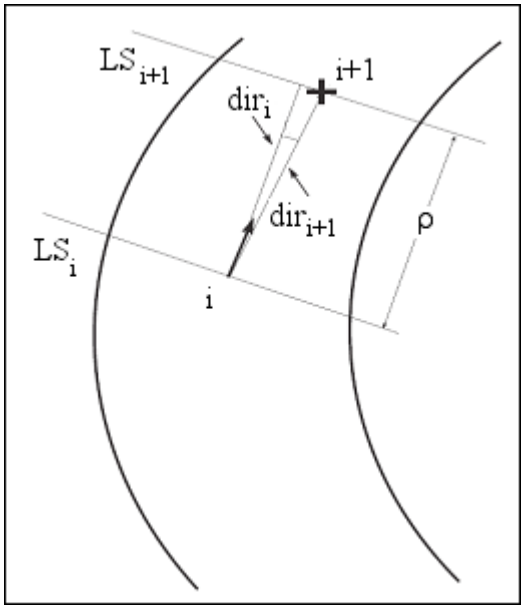

Figure 3.5: Step of the tracing.

3.6 The two-carabinieri technique

As the nerve tracing strategy starts to track nerves from quite a few seed points all over the image, it may result in the splitting of a single nerve into two or more segments, because of the presence of termination situations where the tracking algorithm has stopped. These segments belonging to the same nerve are likely to

have end-points that are close to each other and quite similar with respect to direction, width and gray level intensity. Thus, it was developed a strategy that evaluates all possible pairs of segment end-points, selects the candidates for connection based on their proximity, and decides whether or not to connect these facing end-points by minimizing a weighted combination of the differences in direction, width and gray level intensity of the two segments under exam.
In order to boost correct connections between nerve segments of the same nerve, while at the same time limiting the incorrect ones, an original strategy was devised, in which all remaining pairs of end-points still candidate for connection are evaluated by a more specific analysis. In each pair of end-points, five different arcs are drawn between the two end-points, simulating possible connections (Figure 3.6). The arc composed by image pixels with the brightest average gray level intensity is selected as the candidate connection. Two more arcs, the "carabinieri" (policemen) are then drawn, one on each side of the candidate connection, at a predefined distance, with the aim of controlling (thus the name) the candidate one. If the difference between the (average) gray level intensity of the candidate connection and the (average) ones of the "carabinieri" is larger than an empirically determined threshold, then the candidate connection is accepted as a true connection; otherwise it is rejected.

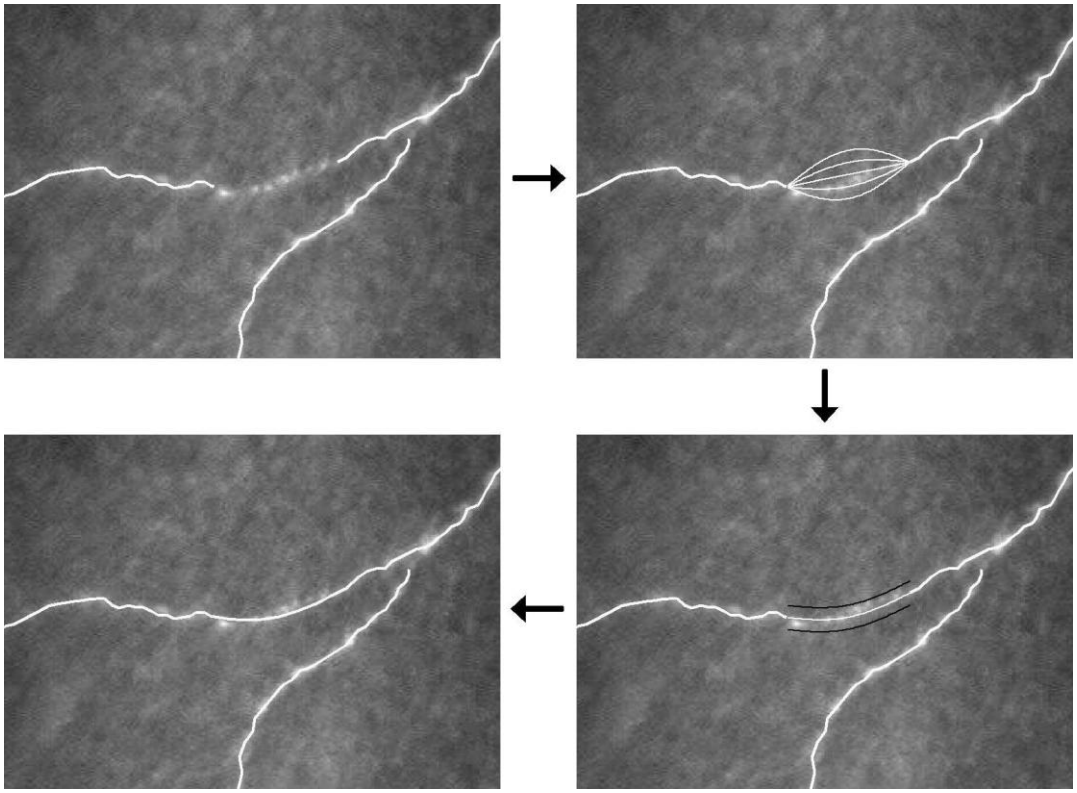

Figure 3.6: The two "carabinieri" (policemen) procedure is used to enhance connection between nerve segments: original image with untracked nerve section (upper left); five arcs to simulate possible connections (upper right); the "carabinieri" arcs (in black), drawn at a predefined distance on both sides of the candidate connection (lower right); the final accepted connection (lower left).

3.7 High-Pass filter

The first improvement is based on a high-pass filtered version of the acquired image, obtained by running a classical 3x3 derivative kernel:

-1	-1	-1
-1	8	-1
-1	-1	-1

Even at first glance, nerves appear much more visible on this latter image (Figure 3.7). The procedure is thus to perform nerve tracking as described in the preceding section and then, using the endpoints of detected nerves, perform an additional tracking on the derivative image. This resulted in a higher percentage of correct nerves recognition, at the expenses of a slightly higher percentage of false recognitions.

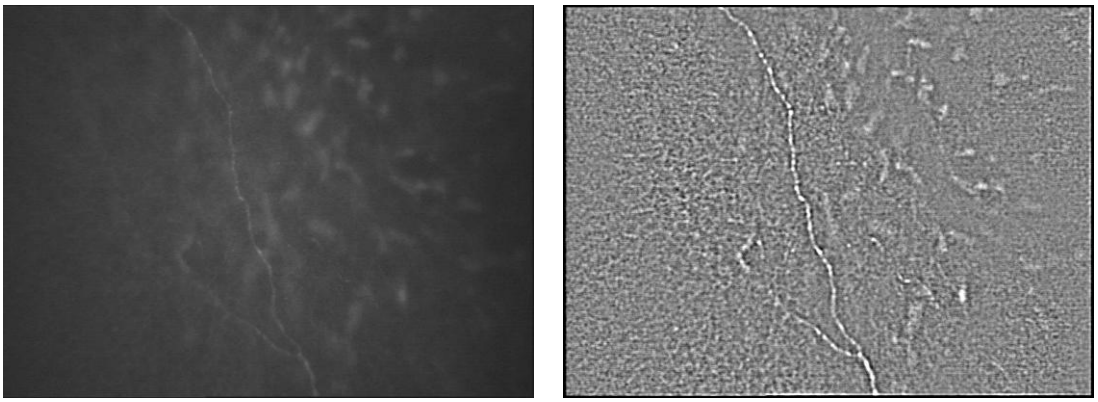

Figure 3.7: Original image and high-pass filtered version.

3.8 False nerve elimination

Improvements are also implemented to reduce the number of false nerve recognitions:

3.8.1 Keratocytes recognition

The vast majority of these false recognitions are due to keratocytes being incorrectly identified as short segments of nerves, as they both appear as bright structures over a darker background. To identify possible keratocytes, the original image was segmented by a simple threshold binarization and the resulting blobs were

then morphologically dilated and eroded. In this segmented image, white blobs may represent either keratocytes or high-luminosity segments of nerves, e.g. nerve beads. Tracked segments inside the former should be deleted, whereas the ones inside the latter should be kept, as they belong to nerves. To this end, tracked segments wholly contained inside white blobs were deleted (as they were assumed to be false nerve recognitions inside keratocytes), whereas longer segments extending also outside white blobs were confirmed (as they were assumed to be true nerve recognitions, in high-luminosity segments).

3.8.2 Internal and external area

False positives are very similar to true nerves when observed locally. However, their non-nerve nature appears evident when the whole nerve is considered. Tracking algorithms follow nerve trajectories typically using small observation windows in order to neglect curvature. This results in a large number of false positives. Grayscale and geometric features can be used to define a classification problem that can be solved using a discriminant analysis. The most obvious features are those related to the luminosity (mean) and contrast (variance) of the nerve and of its local background [32]. A^{int} is defined as the area of image delimited by two nerve borders, and A^{ext} as the background area close to the nerve (Figure 3.8).

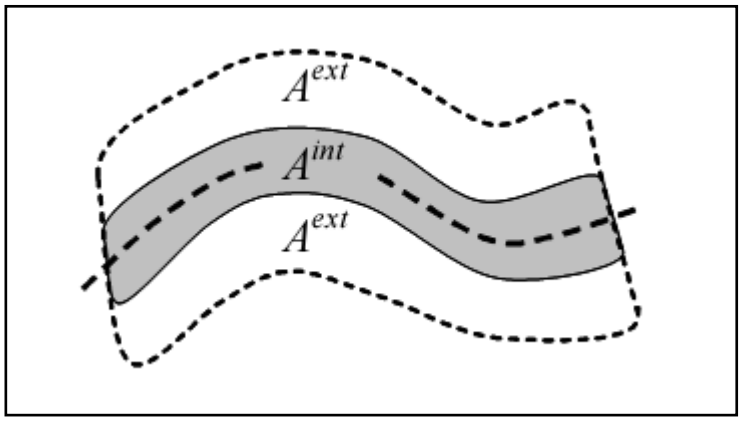

Figure 3.8: The model divides the nerve neighborhood in an internal and external area.

Internal and external average luminosity and contrast are defined as:

$$L^{\text{int}} = \frac{1}{area(A^{\text{int}})} \cdot \sum_{x,y \in A^{\text{int}}} p(x,y)$$

$$L^{ext} = \frac{1}{area(A^{ext})} \cdot \sum_{x,y \in A^{ext}} p(x,y)$$

$$C^{\text{int}} = \frac{1}{area(A^{\text{int}})} \cdot \sum_{x,y \in A^{\text{int}}} \left(p(x,y) - L^{\text{int}} \right)^2$$

$$C^{ext} = \frac{1}{area(A^{ext})} \cdot \sum_{x,y \in A^{ext}} \left(p(x,y) - L^{ext} \right)^2$$

where $p(x,y)$ is the grayscale value of the pixel at x, y. For an ideal nerve $L^{ext} < L^{int}$. The model is therefore extended by adding a third area, the transition (crossing) area A^{cross}, and the corresponding luminosity and contrast features:

$$L^{cross} = \frac{1}{area(A^{cross})} \cdot \sum_{x,y \in A^{cross}} p(x,y)$$

$$C^{cross} = \frac{1}{area(A^{cross})} \cdot \sum_{x,y \in A^{cross}} \left(p(x,y) - L^{cross} \right)^2$$

Intuitively, $L^{ext} < L^{cross} < L^{int}$, as A^{cross} has pixels from both "nerves" and "non-nerves". For the same reason one expects higher contrast C^{cross} compared to C^{int}, C^{ext}. Tracked segments that do not satisfy these equations are considered to be false positive and are deleted.

3.9 Gabor filter

The whole tracking technique described above is then applied also to a version of the images obtained by pre-processing them with a Gabor filter [33], in place of the equalization pre-processing described above. A Gabor filter is a linear filter whose impulse response is defined by a harmonic function multiplied by a Gaussian function. Because of the multiplication-convolution property, the Fourier transform of a Gabor filter's impulse response is the convolution of the Fourier transform of the harmonic function and the Fourier transform of the Gaussian function.

$$g(x, y; \lambda, \theta, \psi, \sigma, \gamma) = \exp\left(-\frac{x'^2 + \gamma^2 y'^2}{2\sigma^2} \right) \cdot \cos\left(2\pi \frac{x'}{\lambda} + \psi \right)$$

where

$$x' = x \cdot \cos\theta + y \cdot \sin\theta$$

and

$$y' = -x \cdot \sin\theta + y \cdot \cos\theta$$

In this equation, λ represents the wavelength of the cosine factor, θ represents the orientation of the normal to the parallel stripes of a Gabor function, ψ is the phase offset, σ is the sigma of the gaussian envelope and γ is the spatial aspect ratio, and

specifies the ellipticity of the support of the Gabor function. The parameters λ, θ, ψ, σ and γ were empirically determined.

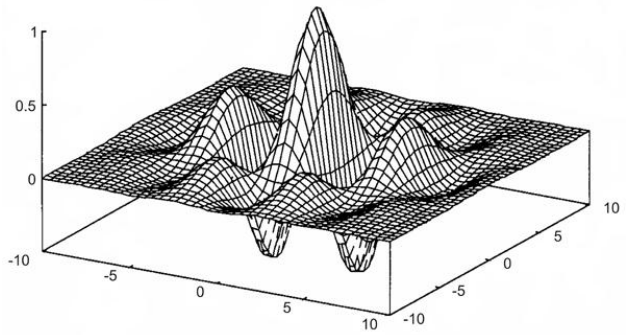

Figure 3.9: Graphic representation of Gabor filter.

With this algorithm, nerve visibility is remarkably enhanced (Figure 3.10) and this allowed overcoming some of the situations where the tracking procedure applied to the equalized images was not able to fully detect a nerve. However, as in some other situations the original equalization technique still yielded better results, we decided to take advantage of both pre-processing procedures, by merging the tracking results obtained by each of them.

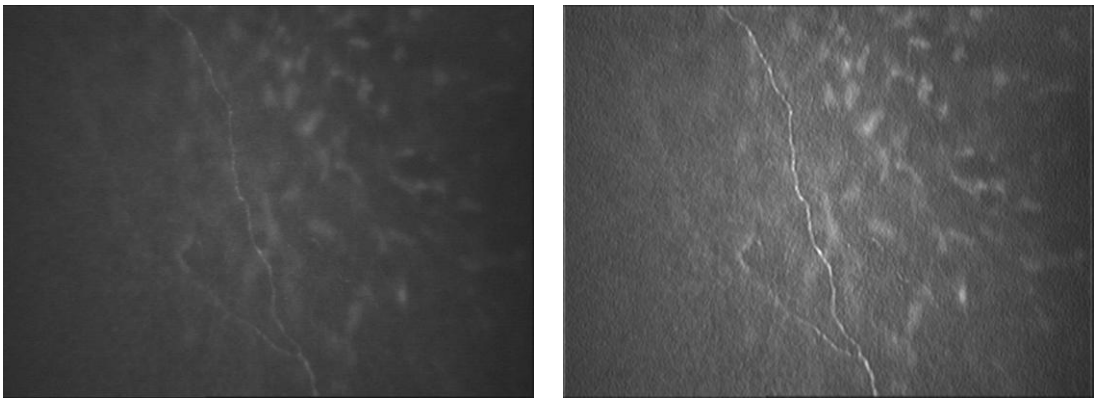

Figure 3.10: Original image and Gabor filtered version
(without luminosity and contrast normalization).

3.10 Performance evaluation

Ninety images of corneal sub-basal epithelium from normal (n=76) and non-normal (n=14) subjects were made available by Nidek Technologies (Padova, Italy) from their own image database. The images were acquired with a confocal microscope (Confoscan4; Nidek Technologies, Padova, Italy), covering a field of 460 x 350 μm^2 at 40X magnification, and saved as JPEG compressed, monochrome, 576 x 768 pixel digital image. All the 90 images of this dataset are publicly available for download [34]. An evaluation of the proposed algorithm was performed on this

data (dataset 1). The manual detection of nerves was performed by tracing all clearly visible nerves with a manual drawing module that was developed ad hoc in the Matlab language. The same images were then analyzed with the proposed algorithm, to provide the automatic detection of nerves.
Because of the curvature of cornea layers and the possibly inaccurate alignment of the instrument on the corneal apex during image acquisition, many of the images also include parts that do not belong to the sub-basal layer (i.e. stroma or epithelium), as shown, for example, in the lower right part of Figure 3.1. To limit the effect of this situation, the detection procedure was then repeated for each image on a user-selected ROI, which was drawn to include as accurately as possible only the portion of the images actually containing nerve structures. Table 3.1 reports the statistics for the length of recognized nerve structures, detected with manual or the automatic method on the whole images or ROIs, for all 90 images and then separately for normal and non-normal images.

Table 3.1: Statistics of detected lengths of nerve structures in the images of dataset nr.1, for whole images or ROIs and using the manual or automatic method.

	Length (μm)	**Whole images**		**ROIs**	
		manual method	**automatic method**	**manual method**	**automatic method**
All subjects (N=90)	**Average**	983	856	974	837
	Std Dev	483	440	480	436
	Min	0	0	0	0
	Max	2522	2024	2503	1959
Normal subjects (N=76)	**Average**	963	829	956	815
	Std Dev	504	451	501	444
	Min	0	0	0	0
	Max	2522	2024	2503	1959
Non normal subjects (N=14)	**Average**	1092	1004	1071	959
	Std Dev	345	352	346	381
	Min	501	539	491	421
	Max	1584	1532	1569	1523

Dividing the detected nerve lengths by images (or ROI) areas, nerve density (in micrometers per square millimeter) were computed and are reported in Table 3.2, for all 90 images and then separately for the normal and non-normal images. The total lengths (density) of nerves are very different in the various images, ranging, for example, from 0 (0 $\mu m/mm^2$) to 2522 (18177 $\mu m/mm^2$) μm by manual method on whole images.

Therefore, reporting absolute values of nerve lengths (density) or of difference between manual and automatic methods is not very informative for quantitative assessment of the performance of the system. A more significant comparison may be performed by considering the percent lengths, namely the ratio of correctly recognized nerves length as a percentage of total length of visible nerves, which is just the sensitivity of the method and the rate of false nerve length recognitions with respect to the total automatically traced length. The latter may be assumed as representative of the specificity of the method, which cannot be computed as the

true-negative nerves are undefined. The results of percent lengths are reported in Table 3.3, still for all 90 images and then separately for the normal and non-normal images. On average, more than 80% of the nerve actually present in an image are correctly recognized, and fewer than 7% of false recognitions are present in the nerves detected by the automatic procedure, with slightly more correct recognitions but also more false recognitions in non-normal images. When the nerve tracing procedure is applied to user-selected ROIs, results are marginally better than on whole images, especially as regards the reduction of false recognition in non-normal subjects.

Table 3.2: Statistics of detected density of nerve structures in the images of dataset nr.1, for whole images or ROIs and using the manual or automatic method.

	Density ($\mu m/mm^2$)	**Whole images**		**ROIs**	
		manual method	**automatic method**	**manual method**	**automatic method**
All subjects (N=90)	**Average**	7088	6171	9033	7772
	Std Dev	3483	3172	3153	2961
	Min	0	0	0	0
	Max	18177	14593	20859	16001
Normal subjects (N=76)	**Average**	6943	5973	8741	7463
	Std Dev	3631	3251	3188	2935
	Min	0	0	0	0
	Max	18177	14593	20859	16001
Non normal subjects (N=14)	**Average**	7875	7240	10621	9445
	Std Dev	2491	2539	2490	2605
	Min	3609	3887	6017	3968
	Max	11416	11044	15064	12285

Table 3.3: Statistics of percent of correctly detected lengths of nerve structures (with respect to manually detected nerves) and of false detection (with respect to total automatically detected nerves) in the dataset images, for whole images or ROIs.

	%	**Whole images**		**ROIs**	
		tracked nerves	**false tracking**	**tracked nerves**	**false tracking**
All subjects (N=90)	**Average**	81.0	6.9	80.4	6.3
	Std Dev	14.4	8.0	14.3	6.2
	Min	36.0	0.0	36.0	0.0
	Max	100.0	44.0	100.0	26.0
Normal subjects (N=76)	**Average**	80.4	6.5	80.2	6.0
	Std Dev	14.6	7.2	14.3	6.1
	Min	36.0	0.0	36.0	0.0
	Max	100.0	32.0	100.0	26.0
Non normal subjects (N=14)	**Average**	83.8	9.1	81.8	7.9
	Std Dev	14.0	11.8	14.7	6.6
	Min	51.0	1.0	48.0	2.0
	Max	100.0	44.0	99.0	25.0

Figure 3.11, Figure 3.12, and Figure 3.13 show the scatter plots of manually versus automatically recognized nerve length in the whole images, for all normal and non-normal images. From this graphic representation of the results, the correlation between the automatic and manual method can be appreciated and quantitatively described by the correlation coefficient, which was 0,94 for all images and 0,95 and 0,86 for normal and non normal-images, respectively. To display the extend of agreement between the two methods, Bland-Altman plots [35] of differences versus average for each pair of manual and automatic lengths in whole images are shown in Figure 3.14, Figure 3.15, and Figure 3.16 for all, normal, and non-normal images, respectively; the lines indicate the average difference and the 95% limits of agreement. Average length differences confirm the moderate underestimation of the automatic method with respect to the manual one: -127 μm (-13%) on all images; -134 μm (-14%) and -88 μm (-8%) in normal and non-normal images, respectively. These differences are uniformly distributed over the whole range of possible lengths, with 95% confidence intervals of -455 μm ÷ 200 μm for all images, and -453 μm ÷ 184 μm, and -463 μm ÷ 287 μm for normal and non-normal images, respectively. Representatives examples of the results obtained by the proposed algorithm are shown in Figure 3.17, Figure 3.18, and Figure 3.19.

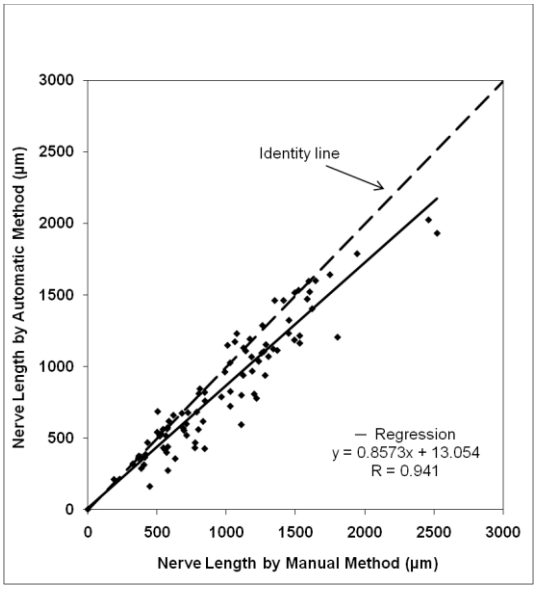

Figure 3.11: Scatter-plot of nerve length from manual vs. automatic method on whole images of all subjects (normal and non normal, N=90) from dataset 1.

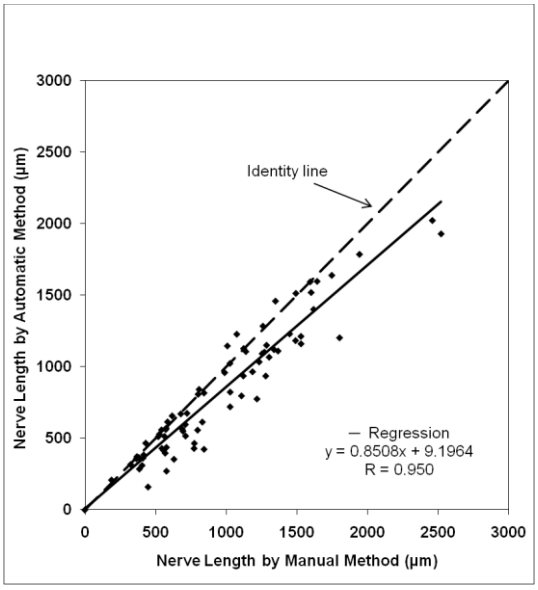

Figure 3.12: Scatter-plot of nerve length from manual vs. automatic method on whole images of normal subjects (N=76) from dataset nr. 1.

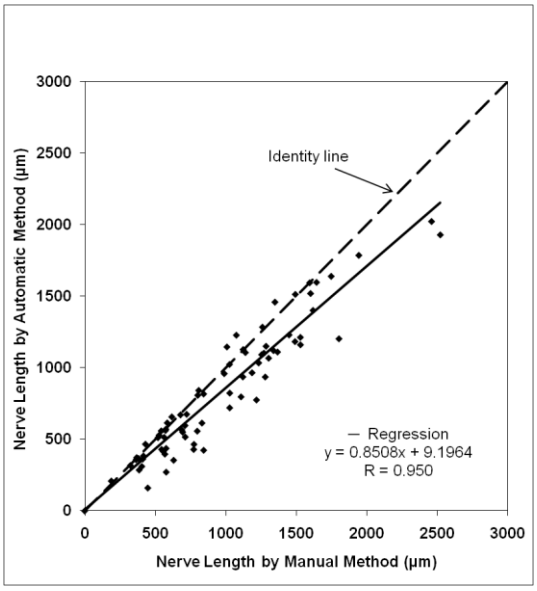

Figure 3.13: Scatter-plot of nerve length from manual vs. automatic method on whole images of non normal subjects (N=14) from dataset nr. 1.

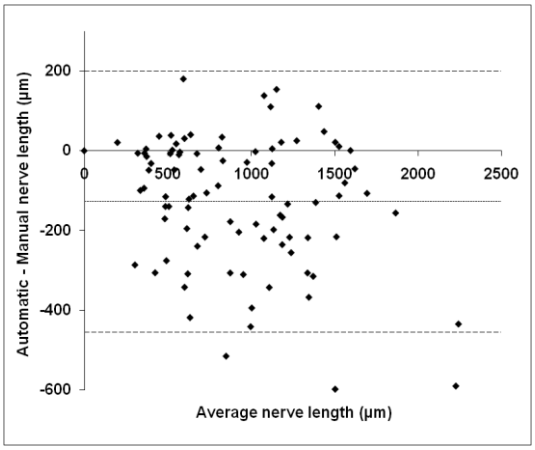

Figure 3.14: Bland-Altman plot for nerve lengths from manual and automatic methods on whole images of all subjects (normal and non normal, N=90) from dataset nr. 1. It displays the difference vs. average for each pair of manual and automatic lengths, with three lines indicating the mean difference (dotted line) and the 95% limits of agreement (dashed lines).

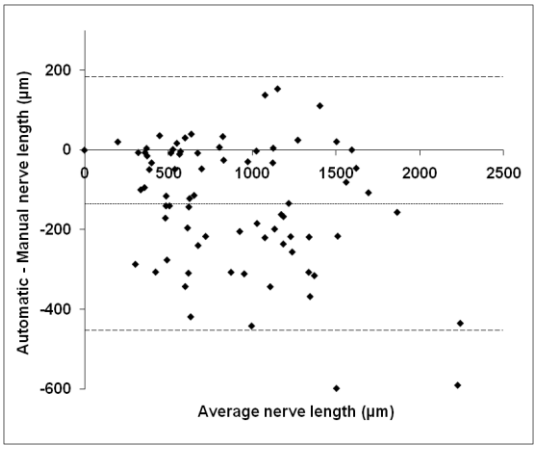

Figure 3.15: Bland-Altman plot for nerve lengths from manual and automatic methods on whole images of normal subjects (N=76) from dataset nr. 1. It displays the difference vs. average for each pair of manual and automatic lengths, with three lines indicating the mean difference (dotted line) and the 95% limits of agreement (dashed lines).

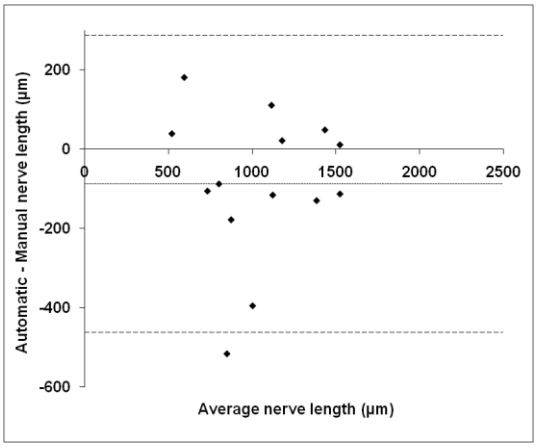

Figure 3.16: Bland-Altman plot for nerve lengths from manual and automatic methods on whole images of non normal subjects (N=14) from dataset nr. 1. It displays the difference vs. average for each pair of manual and automatic lengths, with three lines indicating the mean difference (dotted line) and the 95% limits of agreement (dashed lines).

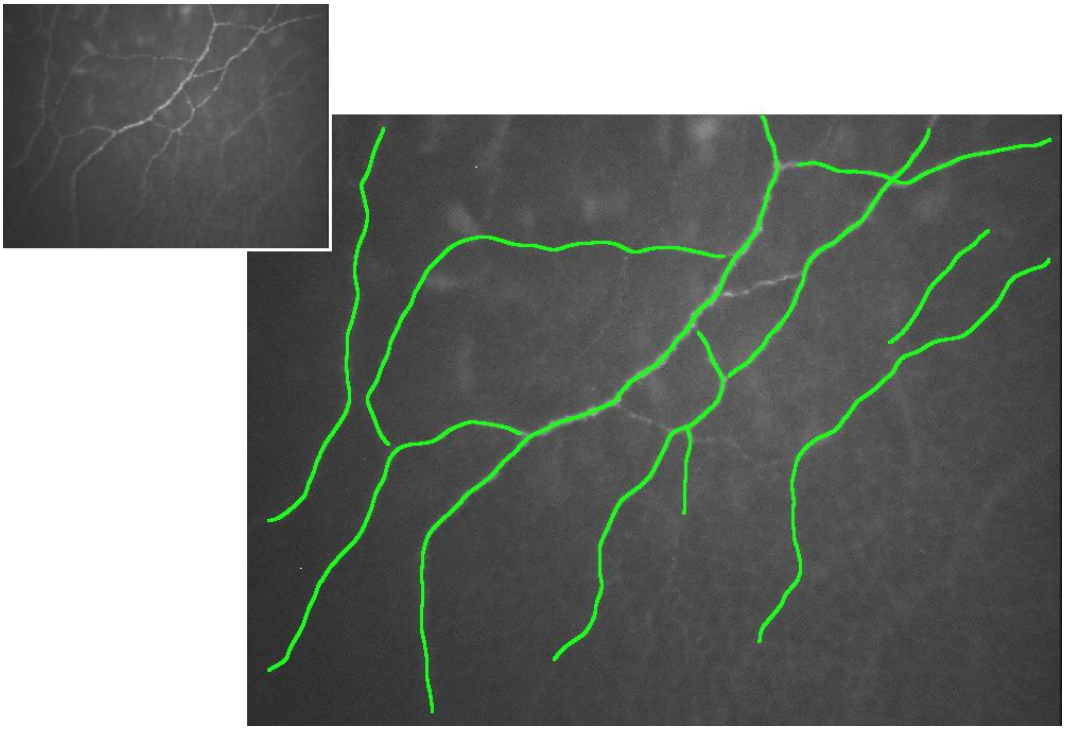

Figure 3.17: Representative result of the nerve tracing technique (original image in the upper left thumbnail).

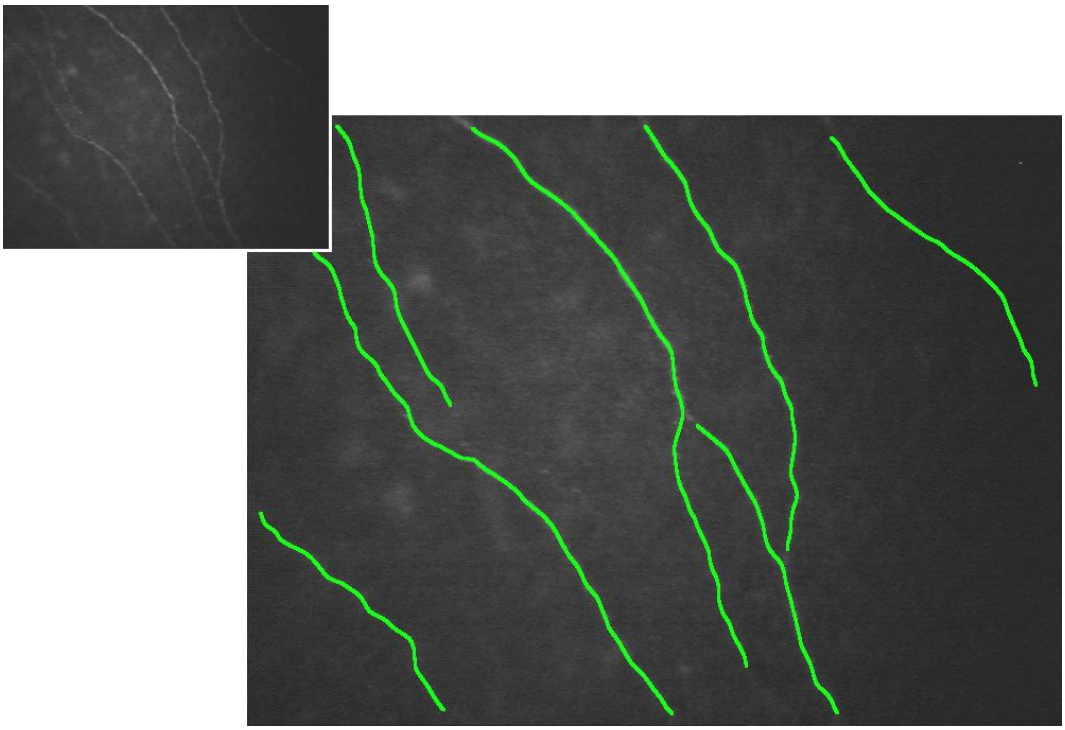

Figure 3.18: Representative result of the nerve tracing technique (original image in the upper left thumbnail).

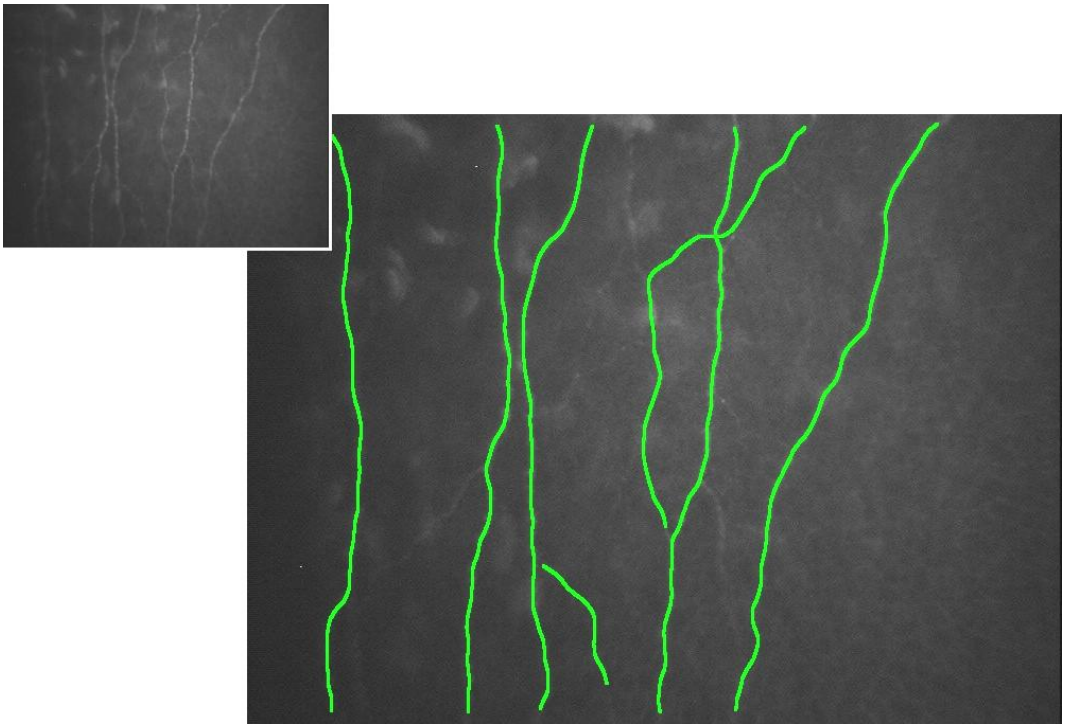

Figure 3.19: Representative result of the nerve tracing technique (original image in the upper left thumbnail).

To confirm these results on images from an independent source, not related to the development of the algorithm presented, we applied the automatic procedure to 80 images from normal subjects (dataset 2) [36], provided, together with the manually determined nerve lengths, by colleagues from the Mayo Clinic College of Medicine (Rochester, MN). A scatter plot and Bland-Altman plot of manually versus automatically recognized nerve lengths in whole images from this dataset are shown in Figure 3.20 and Figure 3.21, respectively. The correlation coefficient between the automatic and manual method for these images is 0,89.

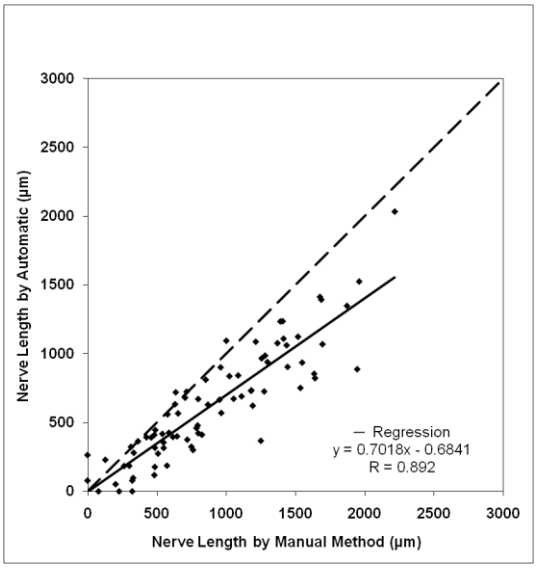

Figure 3.20: Scatter-plot of nerve length from manual vs. automatic method on whole images of subjects from dataset nr. 2, all normal (N=80).

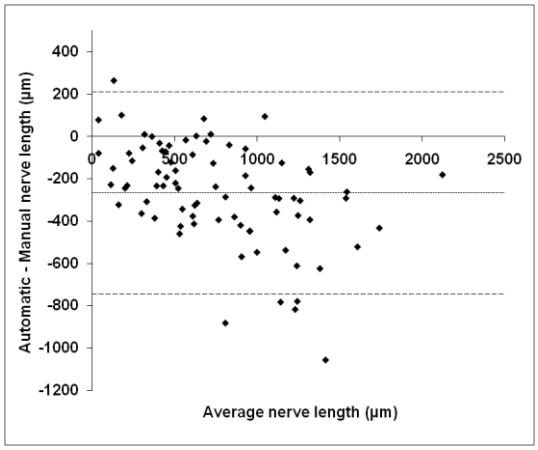

Figure 3.21: Bland-Altman plot for nerve lengths from manual and automatic methods on whole images of subjects from dataset nr. 2, all normal (N=80). It displays the difference vs. average for each pair of manual and automatic lengths, with three lines indicating the mean difference (dotted line) and the 95% limits of agreement (dashed lines).

3.11 Conclusions

The algorithm proposed for nerve recognition is fully automatic, requiring no user intervention. Only if the user wishes to restrict the analysis to a specific ROI, a manual selection of the ROI is performed. The advantage of working on ROIs is that slightly fewer false nerves are detected, at the expenses of a negligible decrease in the percentage of true nerve detection. The overall advantage, however, is quite marginal and, moreover, using a different user-selected ROI in each image would strongly bias the nerve density value.

A very important characteristic of the automatic method is its capability of correctly recovering the differences in nerve length between the various subjects. As shown in Figure 3.11, automatic and manual length estimations in the same image are very well-correlated, both in whole images as well as in ROIs. This ensures that, despite the moderate underestimation of the automatic method with respect to the manual one, shown in Figure 3.14, the former can reliably differentiate between subjects characterized by different nerve lengths.

The performances of the algorithm are affected by the overall quality of the image (e.g. related to luminosity contrast between nerves and background and image noise), and by the possible presence of information partially coming from other layers, whose cell structures (keratocytes, epithelium cells) may be erroneously recognized as segments of nerves. A careful custom setting of the instrument lamp power, an accurate alignment of the system and, at a lesser extent and with the drawbacks mentioned, the adoption of the ROI analysis can certainly improve the performance in these respects.

In view of a clinical application of the algorithm, the possibility of allowing the user to perform some manual touch-up of the automatic results in order to increase the correct nerve detection may also be considered and the proper tools developed. In this way, a manual editing session, of e.g. a few tens of seconds, might allow achieving performances close to 100% of true nerve recognition.

To the author's knowledge, the system presented here is the only ever proposed for the automatic detection of the corneal sub-basal nerve structures. With its application, important clinical parameters such as total length of nerves in the image, nerve density, nerve tortuosity, e.g. evaluated as in [13], could be readily derived in an easy, quantitative and reproducible way. Work is in progress to develop additional computer programs to derive and evaluate the above mentioned clinical parameters. A significant advantage in the clinical assessment of patients can thus be reasonably expected, even if extensive clinical studies, involving a large number of subjects and pathologies, should be conducted to fully assess the overall clinical benefit.

3.12 Further development

A possible improvement of the performance of the algorithm can be achieved by considering not only one image, but all images in the sequence into which sub-basal nerve fibers are visible. A preliminary attempt was made taking 5 images (Figure 3.22) of 1 sequence, and a new image is obtained by averaging these 5 images (Figure 3.23).

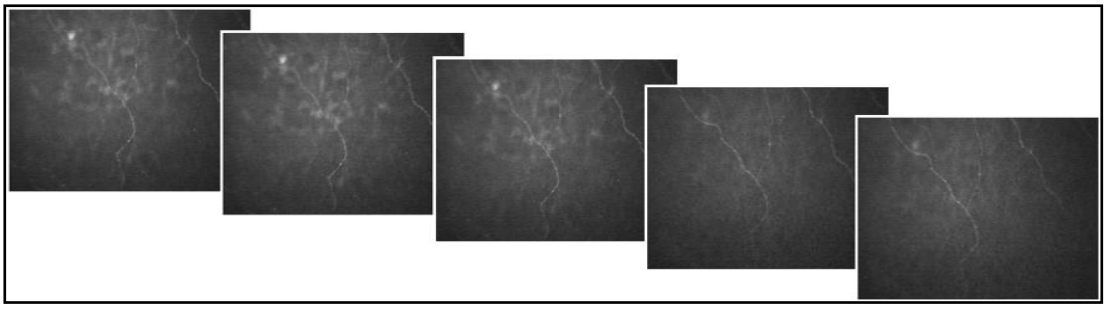

Figure 3.22: All the images of a sequence containing nerves.

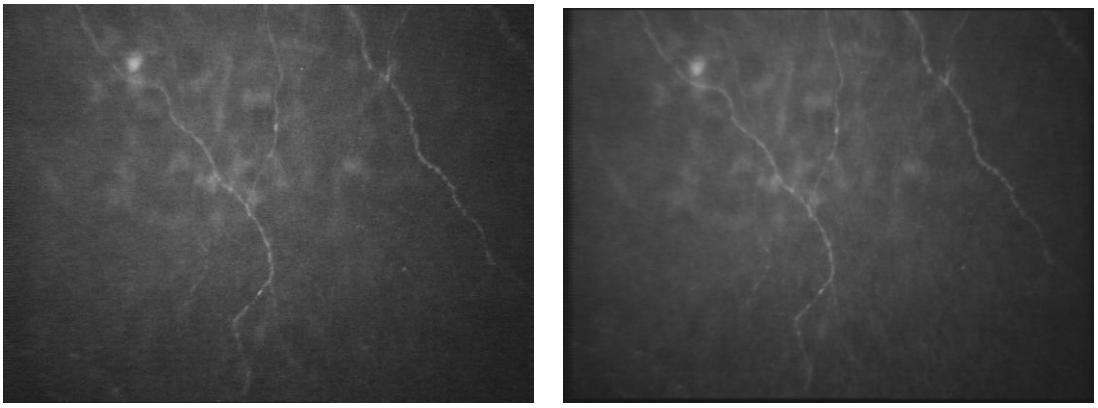

Figure 3.23: original image and average version.

Automatic tracking achieves a better result on the average image (Figure 3.24), where the percentage of correct nerves recognition is higher.

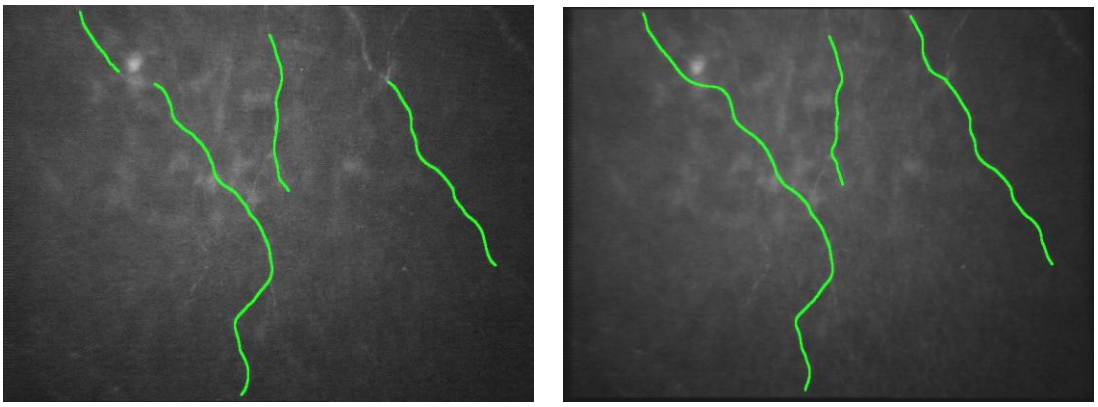

Figure 3.24: tracing performed on the original image and on the average image

Chapter 4

3D Reconstruction and Keratocyte Density Estimation

4.1 Materials

Analyzing corneal structures, e.g. keratocytes, in the whole volume of the cornea and not only in a layer at a specific depth has been shown to be quite important [14, 15]. Keratocytes are present in the full thickness of stroma, their nuclei are visible as bright objects (the cell bodies are larger and usually not visible) against the dark background of the extracellular tissue (Figure 4.1), and their density is an important clinical parameter. Keratocytes are fibroblast-like cells that maintain the health and clarity of the corneal stroma.

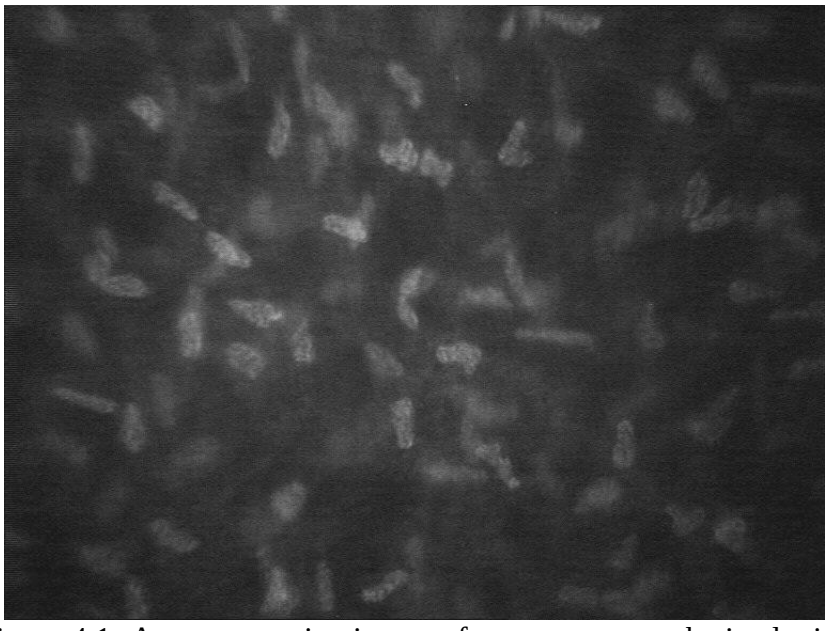

Figure 4.1: A representative image of cornea stroma obtained with the ConfoScan 4 confocal microscope (Nidek Technologies, Italy).

Several investigators have examined changes in density of these cells with age [17], with contact lens wear [18], after refractive surgery [20, 21], and after corneal transplantation [22]. Some researchers attempted to identify and count cells in the stroma automatically [53, 54, 55]. Currently this density is calculated on the 2D images, but stroma represents, on average, 80% to 90% of the whole corneal volume and it is important to analyze the 3D arrangement and density of stromal keratocytes [24]. A program that identifies and selects cells in confocal images would be more objective than manual assessment of low contrast images.

The purpose is to provide a three-dimensional reconstruction (starting from a sequence of 2D images) that allows visualization and analysis of all corneal structures in the 3D volume, and the automatic estimation of the keratocytes volumetric density.

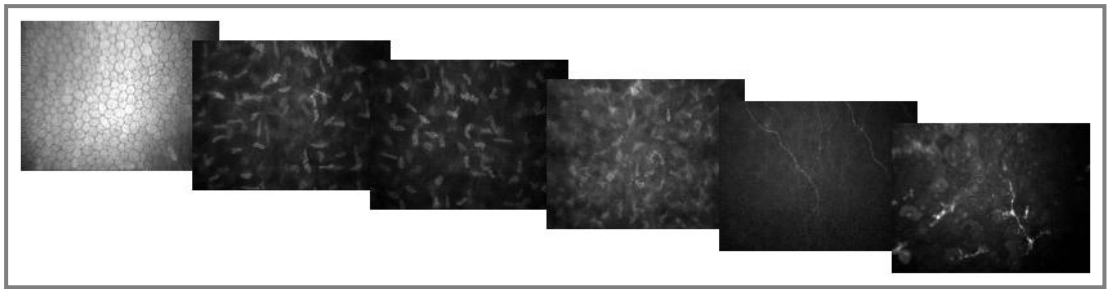

Figure 4.2: A representation of a sequence of images, from endothelium to epithelium

Sequences of images (Figure 4.2) covering the whole thickness of the cornea (from endothelium to epithelium) were acquired in normal subjects with the Confoscan4 confocal microscope (Nidek Technologies, Italy). In order to increase image stability and to have a precise location along z-axis, we acquired images using the "Z-Ring system", a positional sensor that is in contact with the eye. The acquisition of each sequence required about 15 seconds. Each image covers a field of 460x350 μm in the x-y plane, it is acquired at 40X magnification and saved as a monochrome 768x576 pixel digital image. Along the z direction, the position of each image is known but the step (distance between two adjacent images) is not constant: e.g. in a sequence of 144 images, the step can vary from 1 μm to 6 μm, with an average of 4 μm.

4.2 Image enhancement

Acquired images do not usually have a uniform luminosity and contrast, exhibiting darker areas in the peripheral regions of the image. This is due to many factors, including the spherical shape of corneal layers, which causes a non uniform reflection of illumination light in the different corneal areas, and the different attenuation of light along the various illumination paths. In order to compensate for this and to reduce the blur present in the image, a band-pass frequency filter is applied to each image. The band-pass filter adopted has cut-off

frequencies of $0.02f_c$ and $0.2f_c$ where f_c is the spatial sampling frequency of the image. Intensity is then adjusted using a sinusoidal transformation curve. In pre-processed images, blur appears attenuated and corneal structures are more visible, even in the dark peripheral areas of the image (Figure 4.3).

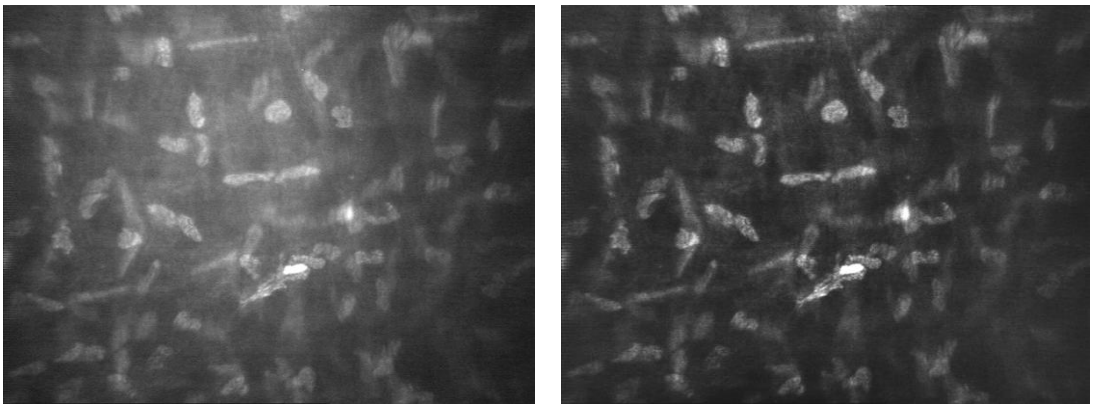

Figure 4.3: Original image and Pre-processed version.

4.2 Registration procedure

Movements of the cornea due to cardiac pulse, respiration or other factor imply that images are misaligned and shifts in the x-y plane may take place within the image stack. Usually, these shifts are just a few pixels (from 0 to 3 μm), but larger shifts (more than 10 μm) are sometimes present. While movements in the x-y plane are often presents, no rotation movement was noticed and thus rotation is not addressed by the registration procedure. In order to compensate for these movements, a completely automatic registration procedure is applied. Registration is performed between each pair of images in the sequence and it consists of the following steps:

1. identification of two ROIs (Regions Of Interest, 120x120 pixels) in the first image, having the highest brightness and contrast. The purpose is to select two ROIs that may lead to a good match in the next image.

2. a correlation method is used to calculate the shifts required along x- and y-axis to obtain the position of the best match of the two ROIs in the second image. The correlation operation can be seen as a form of convolution:

$$corr = \sum_{i=1}^{N} I_i M_i$$

the intensity (M_i) of the N pixels of the ROI is multiplied by the intensity (I_i) of the N underlying image pixels (the next image). The result increases if the image gets brighter: the solution is to use the normalized correlation [37]:

$$corr = \frac{N \cdot \sum_{i=1}^{N} I_i \cdot M_i - \sum_{i=1}^{N} I_i \cdot \sum_{i=1}^{N} M_i}{\sqrt{\left(N \cdot \sum_{i=1}^{N} I_i^2 - \left(\sum_{i=1}^{N} I_i \right)^2 \right) \cdot \left(N \cdot \sum_{i=1}^{N} M_i^2 - \left(\sum_{i=1}^{N} M_i \right)^2 \right)}}$$

With this expression, the result is unaffected by linear changes (constant gain and offset) in the image or model pixel values. The result reaches its maximum value of 1 where the image and model match exactly, gives 0 where the model and image are uncorrelated. The two ROIs are registered separately. Under the reasonable assumption that the shifts between two adjacent images are small, at first only a small region of second image is examined: if a good correlation is not found, a larger region is considered (moving on until a good result is obtained or the whole image is examined).

3. comparison between the registrations separately obtained for the two ROIs: if x and y shifts calculated for the first ROI are not the same of those calculated for the second ROI (with a tolerance of one pixel), that registration is considered a failure. In this case, x and y shifts are set to 0 and the user is informed. When this automatic registration procedure failed, even using a manual method it is very difficult or even impossible to find a match between the two images.

4.3 3D visualization

The stack is reconstructed by taking into account shifts along x, y and z directions (Figure 4.4). Shifts along x and y directions come from the registration process, shift along z direction comes from the Z-Ring sensor.

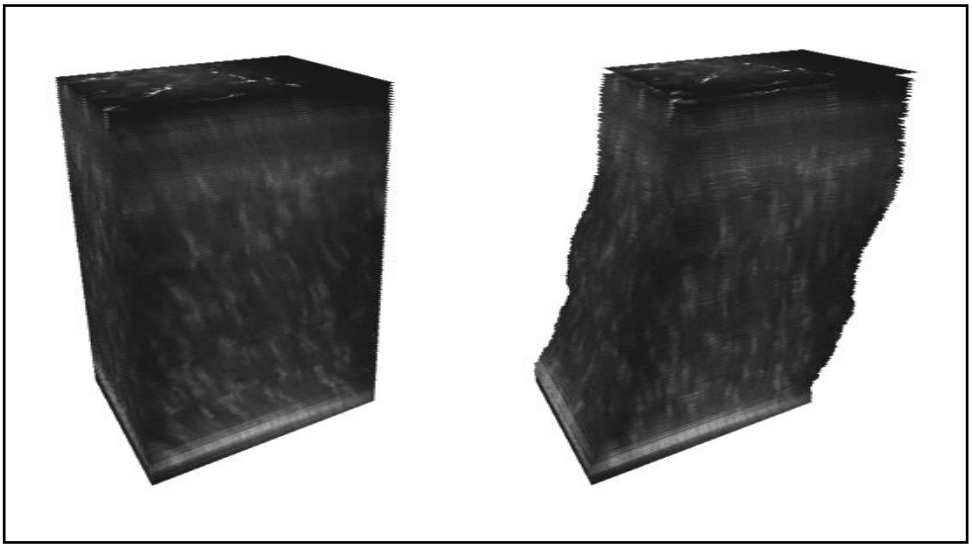

Figure 4.4: Reconstructed stack without and with shifts along x and y directions. In the image on the left the step between an image and the next one is assumed to be constant (4 μm). In the image on the right, each slide is at its real position along z (the step vary from 1 μm to 6 μm, with an average of 4 μm). Sequence of 144 images (from endothelium to epithelium), with a total thickness of 580 μm

The stack is used to generate the 3D reconstruction and to visualize 2D images from any x, y and z directions, taking a line from each image [38]. Reconstructed 2D images from x and y directions may present some missing lines: this is due to the fact that the distance along z between two adjacent images (step) may be more than one pixel. The step is calculated from the z-axis position of images, which, as remarked before, is known but not constant along the whole sequence (it depends on the focal plane speed, derived from the lens movements speed by a nonlinear equation). The reconstruction of the missing lines is made by interpolating the nearest known lines, using a weighted mean:

$$I(x, y_i) = \frac{w_1 \cdot I(x, y_1) + w_2 \cdot I(x, y_2)}{w_1 + w_2}$$

where $I(x,y)$ is the intensity of the pixel located at (x,y) coordinates, y_i is the y coordinate of the missing line $(y_1 < y_i < y_2)$, y_1 is the y coordinate of the lower known line, y_2 is the y coordinate of the upper known line, w_1 and w_2 are weights:

$$w_1 = \frac{y_2 - y_i}{y_2 - y_1} \qquad w_2 = \frac{y_i - y_1}{y_2 - y_1}$$

An example is shown in Figure 4.5.

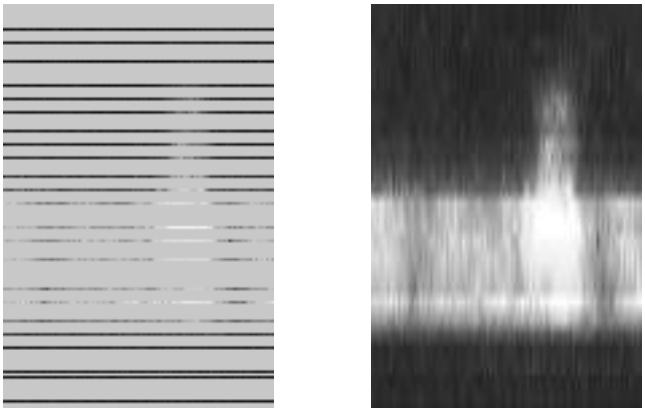

Figure 4.5: Images before (left) and after (right) interpolation (side view from x direction, in the y-z plane, 100x150 pixel).

It is possible to display images related to any side view from x, y, or z directions. The side view from the x direction (in the y-z plane) is the reconstructed 2D image that consists of a column from each image in the sequence at a x-axis position selected by user (Figure 4.6). The side view from the y direction (in the x-z plane) is the reconstructed 2D image that consists of a row from each image in the sequence at a y-axis position selected by user (Figure 4.7). The side view from z direction (in the x-y plane) is the original image at a z-axis position selected by user (Figure 4.8). It is also possible to display a 3D object that represents three images related to the three side views. In this case, the position in the 3D volume of each image is visible (Figure 4.9). The 3D object can be rotated, zoomed, and translated. The position along x, y, and z directions can be freely changed by the user, and images and 3D objects are refreshed in real time according to the new position.

The 3-D reconstruction makes the keratocytes appear quite thick (z dimension), when in fact they are only a few µm thick. Their thicker appearance is an artifact of the depth of field of the confocal microscope.

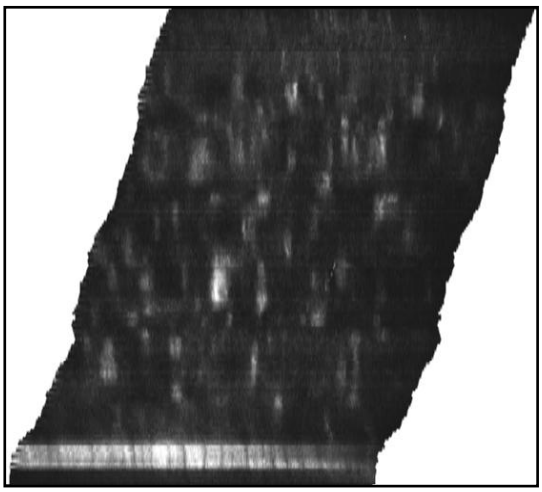

Figure 4.6: Side view from y direction, in the x-z plane, 1114x1005 pixel.

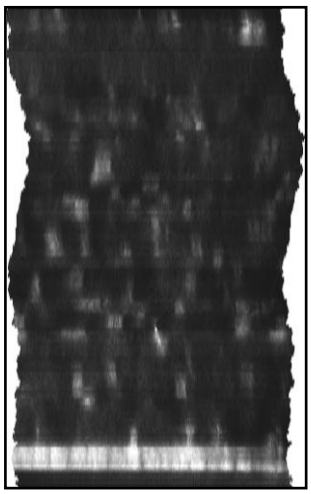

Figure 4.7: Side view from x direction, in the y-z plane, 628x1005 pixel.

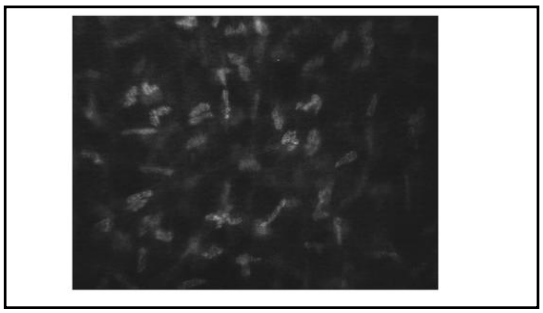

Figure 4.8: Side view from z direction, in the x-y plane, 628x1114 pixel. This image is the original image shifted according to x and y shifts.

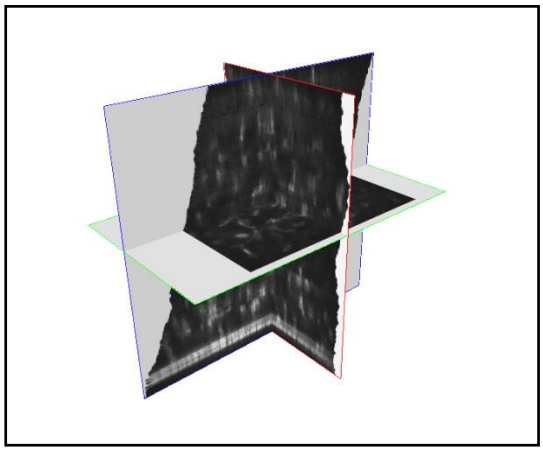

Figure 4.9: 3D object. It represents the three side views with respect to their position in the 3D volume.

4.4 Keratocyte recognition

All the images in each sequence were registered to compensate for possible x-y shifts, in order to obtain a 3D stack of z-aligned images. A fixed ROI is selected (135<x<612, 10<y<566), in order to exclude the peripheral areas of the image, the darker areas (Figure 4.10).

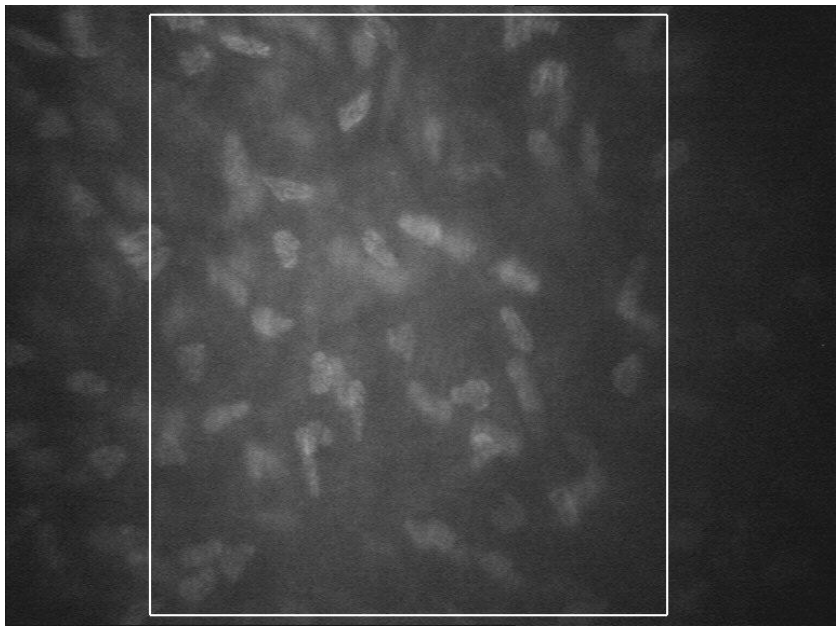

Figure 4.10: Fixed ROI selection.

In order to enhance corneal structures and to reduce the blur presents in the image, a band-pass frequency filter is applied to the fixed ROI (Figure 4.11). A custom segmentation procedure is applied to each image to detect keratocyte 2D contours: it consist in a threshold applied to partially overlapping blocks. The value of the threshold is computed using a modified Otsu technique [39]. After the threshold application, the binary image still contain unwanted noise. Thus, a series of mathematical morphology operations (dilation and erosion) remove very small objects, smooth boundaries, and fill gaps in objects. Objects are then grouped by using a connected component analysis (figure 4.12).

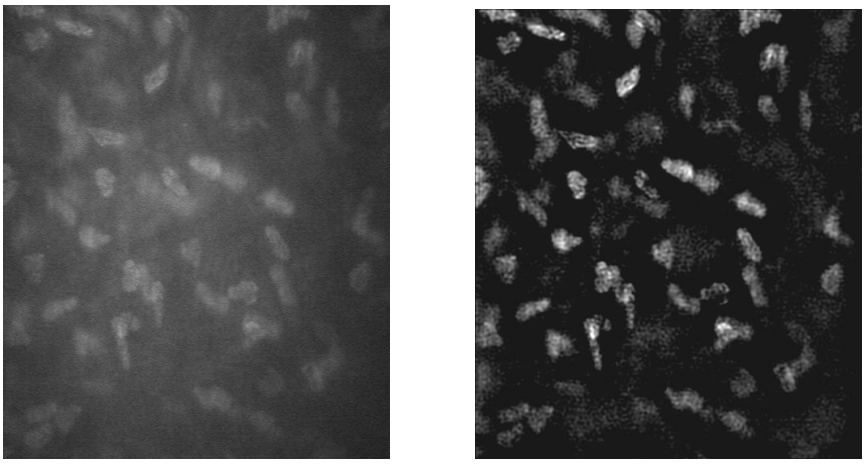

Figure 4.11: Keratocytes recognition: original image and enhanced version

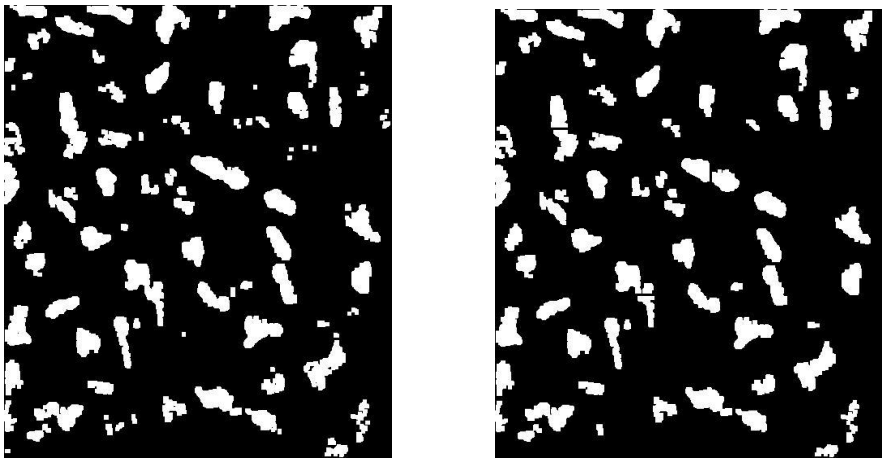

Figure 4. 12: Keratocytes recognition: binary image (on the left) and binary image after morphological operations (on the right).

Due to the small step along z and to the depth of field, each keratocyte appears in more than one image of the sequence. Once that keratocytes are recognized in each image, a clustering procedure is applied to the images of each stack, so as to identify the 3D contour of keratocytes. The purpose of the clustering procedure is to establish if a keratocyte found in one image is the same keratocyte found in the previous image or in the following image. The clustering procedure is based on the distance

between keratocytes of different images, along x, y and z directions. 3D center of keratocytes are then found (Figure 4.13).

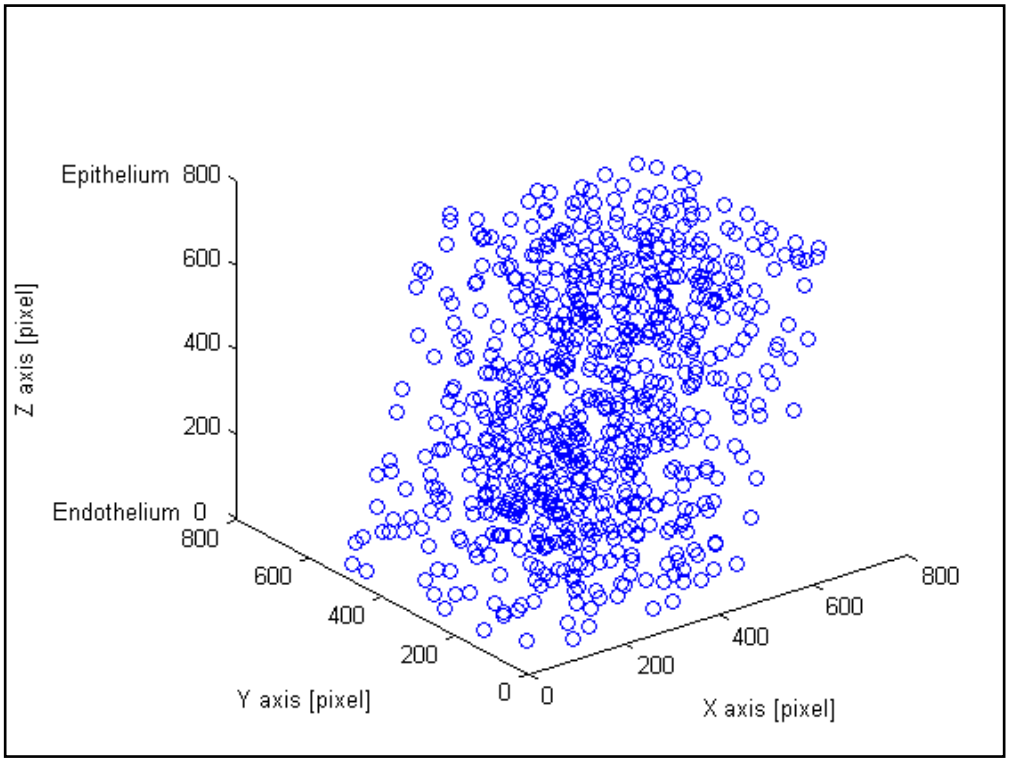

Figure 4.13: 3D center of keratocytes; only images from the stromal part of the sequence (containing no epithelial nor endothelial cells) are used. Sequence of a normal subject.

4.5 Keratocyte density

Each stack of images is then partitioned into 5 adjacent layers [20] (Figure 4.14):

- anterior stroma (0%-10% of stromal depth);
- anterior mid stroma (11%-33%);
- central mid stroma (34%-66%);
- posterior mid stroma (67%-90%);
- posterior stroma (91%-100%);

Stromal thickness is defined as the distance between the first focused image of the most anterior keratocytes and the last focused image of the posterior keratocytes.

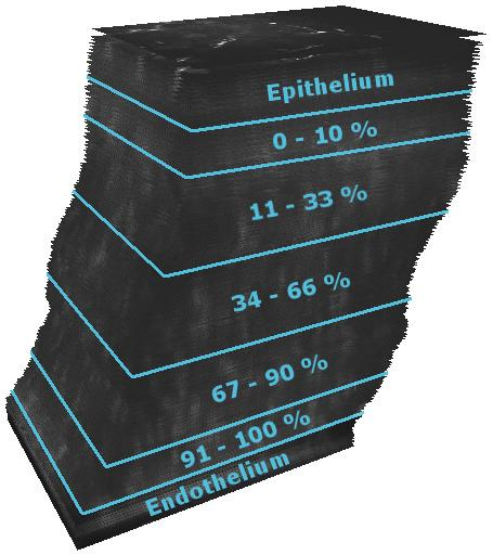

Figure 4.14: Schematic representation of the five stromal layers.

3D centers of keratocytes are counted in each layer (see the following figures), to estimate their volumetric density.

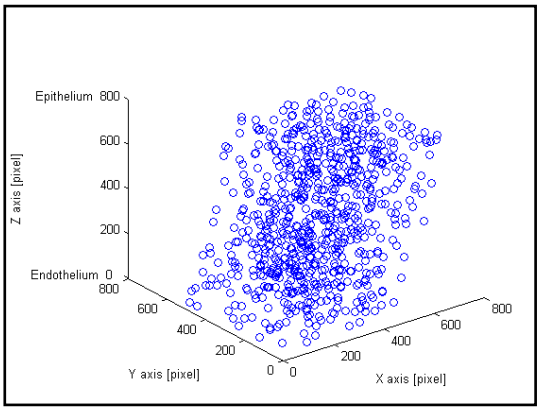

Figure 4.15: 3D keratocytes centers.

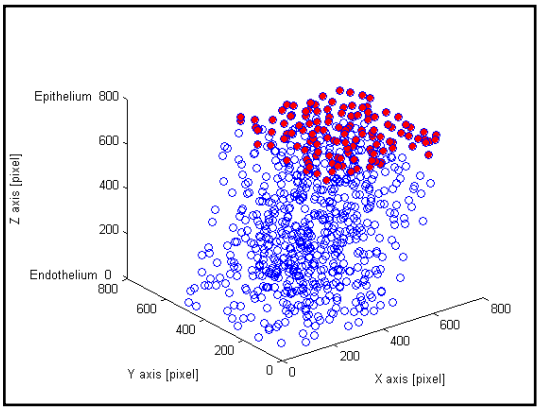

Figure 4.16: 3D keratocytes centers in the anterior stroma.

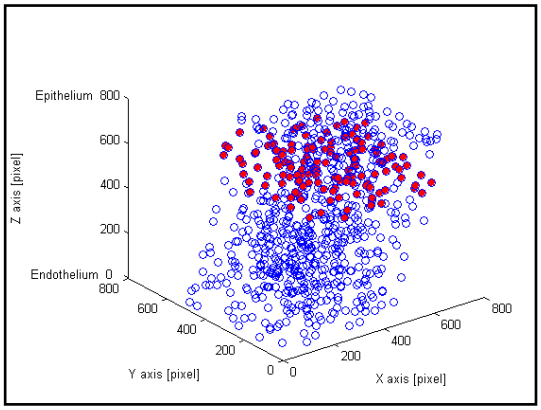

Figure 4.17: 3D keratocytes centers in the anterior mid stroma

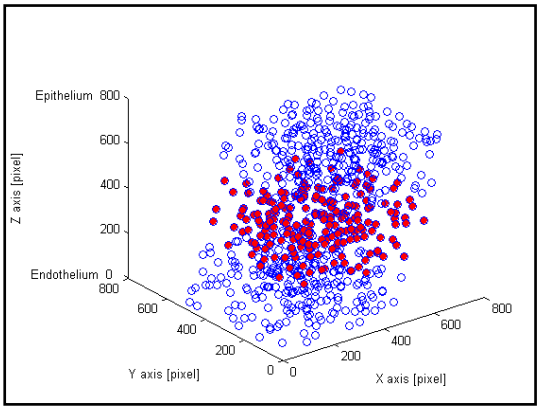

Figure 4.18: 3D keratocytes centers in the central mid stroma

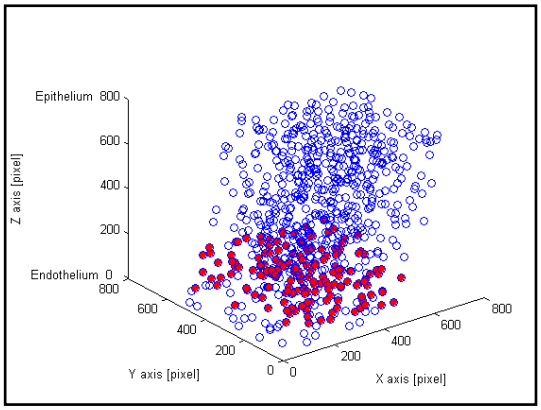

Figure 4.19: 3D keratocytes centers in the posterior mid stroma

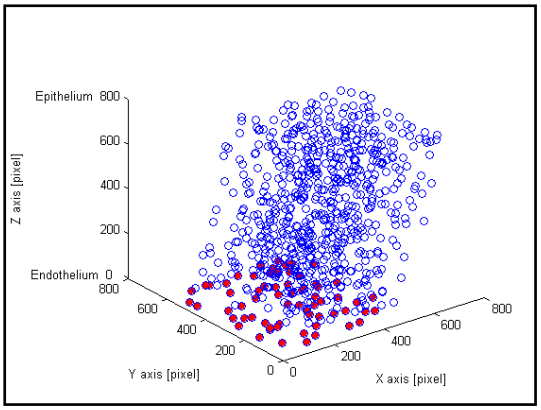

Figure 4.20: 3D keratocytes centers in the posterior stroma

For each layer, keratocyte density is define as:

$$\text{density} = \frac{\text{number of keratocytes in the layer}}{\text{volume of the layer}}$$

4.6 Performance evaluation

Sequences of 3 normal subjects were made available by Nidek Technologies from their own image database. Keratocyte densities were estimated in these 3 normal subject (Table 4.1). 101 stroma images were analyzed in subject nr. 1, 68 in nr. 2, and 103 in nr. 3.

Table 4.1: automatic keratocyte density

Layer	Keratocyte Density [cells / mm^3]		
	Subject 1	**Subject 2**	**Subject 3**
Anterior Stroma	36361	32600	30105
Mid Anterior Stroma	18274	18941	19691
Mid Central Stroma	20416	15932	17286
Mid Posterior Stroma	21851	18117	18410
Posterior Stroma	22992	19064	16589

To obtain ground truth values of densities to compare with, manual detection of keratocytes on each 2D image and then on the 3D stacks of images was also performed. Manual keratocyte density estimation was performed in the 3 normal subjects (Table 4.2). It is however quite difficult and time consuming to obtain reliable manual estimations of volumetric keratocyte densities.

Table 4.2: manual keratocyte density.

Layer	Keratocyte Density [cells / mm^3]		
	Subject 1	**Subject 2**	**Subject 3**
Anterior Stroma	38725	28923	26678
Mid Anterior Stroma	18812	19498	19803
Mid Central Stroma	19584	16698	16980
Mid Posterior Stroma	21464	17904	20325
Posterior Stroma	21678	20971	14413

The percent differences between automatic keratocyte densities and the corresponding manual ones are reported in Table 4.3 for the 5 layers in each subject. In this limited data set of normal images, very good average automatic vs. manual differences were obtained (range: -2.9%; 6.5%). The least accurate estimations were obtained in the peripheral layers of stroma, with a maximum individual difference of 15% [40].

Table 4.3: Percent differences between automatic keratocyte density and the corresponding manual one.

Layer	Subject 1	Subject 2	Subject 3	Average
Anterior Stroma	-6.1	12.7	12.8	6.5
Mid Anterior Stroma	2.8	-2.8	-0.6	-2.1
Mid Central Stroma	4.2	4.6	1.8	3.5
Mid Posterior Stroma	1.8	-1.2	-9.4	-2.9
Posterior Stroma	6.0	9.0	15.0	4.0
Average	0.6	0.9	3.9	1.8

Keratocyte density was automatically estimated in 20 subjects (table), normal and non-normal, but manual estimation of keratocyte density in these 20 subjects was, at present, not performed. However, automatic keratocyte density is reported in the following Table 4.4 and in the corresponding Figure 4.21.

Table 4.4: automatic keratocyte density (mean ± standard deviation)

Layer	Keratocyte Density [cells / mm^3]
Anterior Stroma	29874 ± 8539
Mid Anterior Stroma	21312 ± 3563
Mid Central Stroma	19731 ± 4420
Mid Posterior Stroma	19701 ± 3268
Posterior Stroma	20127 ± 5387

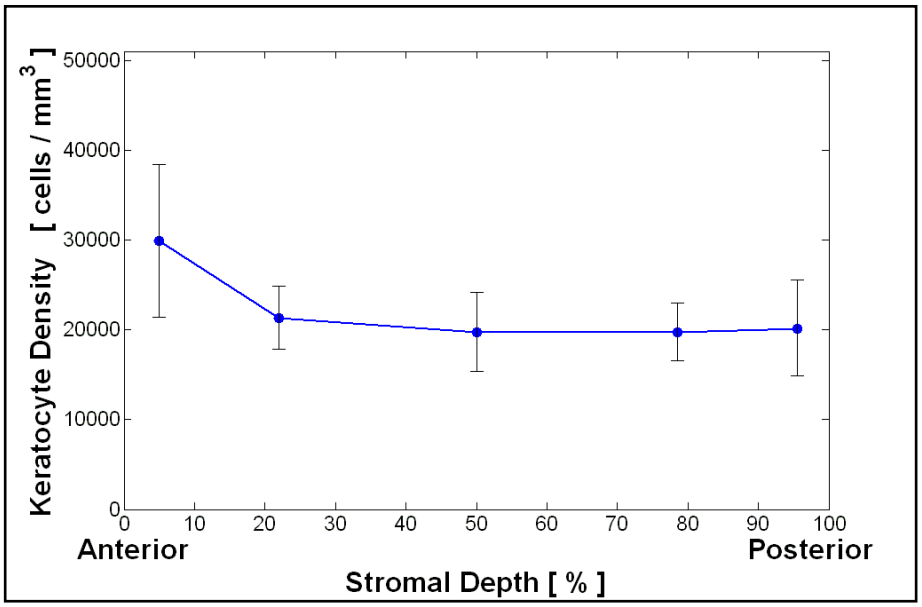

Figure 4.21: automatic keratocyte density (mean ± standard deviation)

4.7 Conclusions

In this thesis, a fast, reliable and easy to use tool to visualize corneal structures was developed. It is possible to locate each structure and layer in the 3D volume and to visualize each image in the exact position along x, y, and z directions. The side views from x and y directions are an important result in in-vivo corneal confocal microscopy. At present, this tool is intended for visualization purposes only, but improvements in patient clinical assessment are already achievable.

Registration is the most important part of the algorithm and to the best of our knowledge it allows for the first time the in-vivo 3D reconstruction of the human cornea. It failed in 3% of images. The reasons for these failures were a large distance along the z direction between the two images examined (in this case, the two images did not have common features) and poor image quality (images very dark and with no visible structure). The difference between automatic and manual registration is on average 1.5 pixels, which is the same difference between manual registrations made by two different human experts. An interesting example of registration is shown in Figure 4.22: large movements of the patient were present during acquisition, but our algorithm was able to reconstruct the correct position of each image.

We noticed in all reconstructed stacks that shifts were mainly located in the x direction and that there was a large shift (about 100-150 μm) towards right for both the left and right eye: until now, these aspects had never been noticed. This shift may be due to a misalignment of the instrument during acquisition, but the issue is worth investigating.

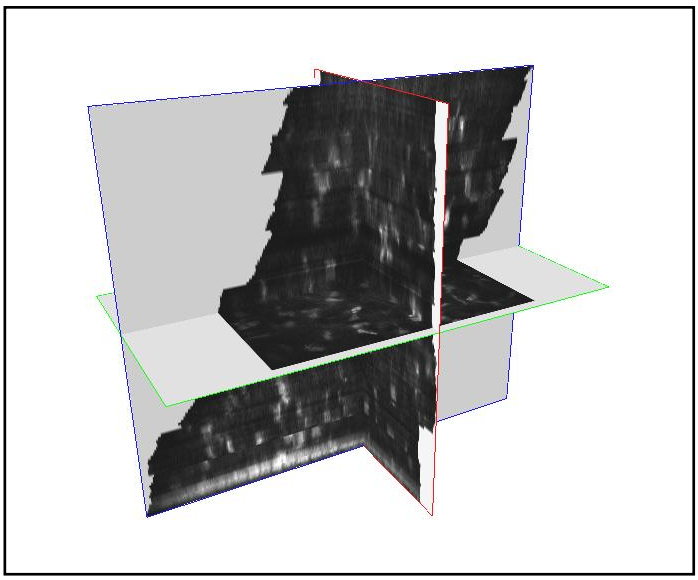

Figure 4.22: 3D object. It is the 3D reconstruction from a sequence of 127 images.

The 2D image to be displayed may not lie along the orthogonal axes of 3D volume, but be along a plane oriented at some oblique angle to the orthogonal axes of the volume image. Oblique images are less intuitive and their visualization is not yet implemented.

Each image captured with confocal microscope represents a 2D picture of a slice of cornea, hypothetically with an infinitesimal thickness. The actual thickness in each image is on the contrary about 25 μm (nominal value) and thus adjacent layers affect the acquired image [41]. This effect is quite visible in the side views from x and y directions, where the thickness of structures of the cornea often appears larger than expected from anatomy. Image restoration techniques, such as blind deconvolution [42], can be applied along the z direction to remove this effect.

With regard to keratocyte density estimation, in the data set of 3 normal images, very good average automatic vs. manual differences were obtained (range: -2.9%;

6.5%). The least accurate estimations were obtained in the peripheral layers of stroma, with a maximum individual difference of 15%. An extensive evaluation will be performed in a larger set of CS4 sequences, including also pathological subjects, albeit obtaining reliable manual estimations of volumetric densities is quite difficult and time consuming.

Work is in progress to improve the segmentation procedure to better detect 2D contour and center of keratocytes. A first attempt was made using the GVF (Gradient Vector Flow) [43], and the result on a 2D image is shown in Figure 4.23.

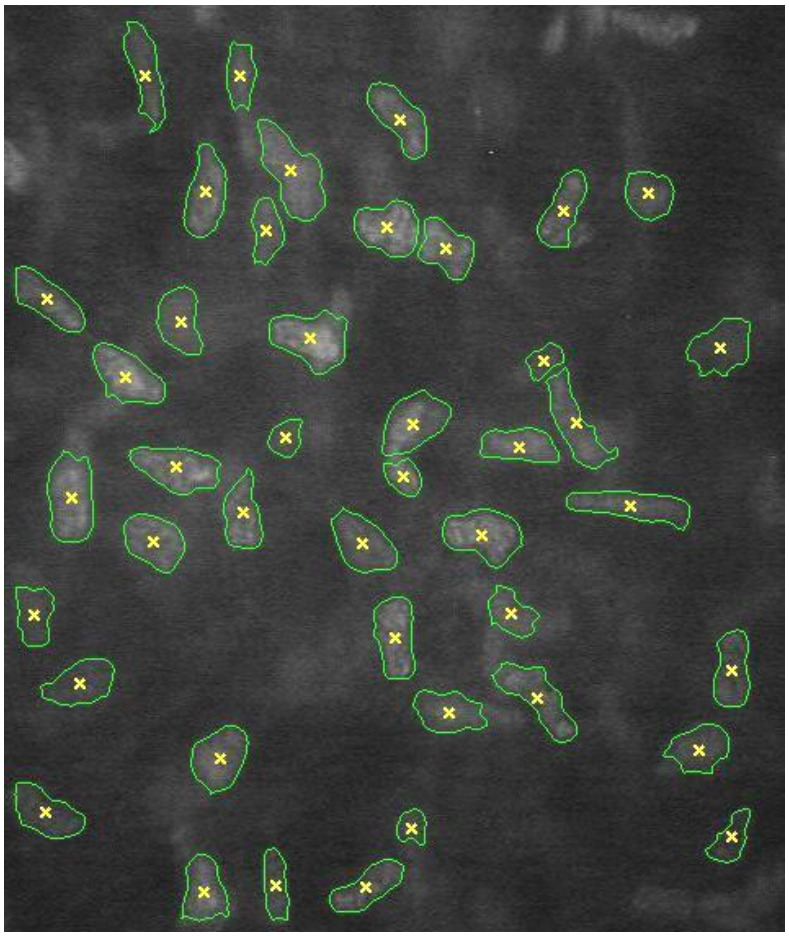

Figure 4.23: 2D contour and center of keratocytes, found using the GVF.

Chapter 5

Cell Contour Detection

5.1 Materials

The analysis of microscopy images of corneal endothelium (Figure 5.1) is quite important to assess cornea health state and quality. Clinicians are interested in determining cell density and cell morphology [25, 26, 27], since these features can be used as early indicators of corneal pathologies or in the typing of corneas for possible transplants.

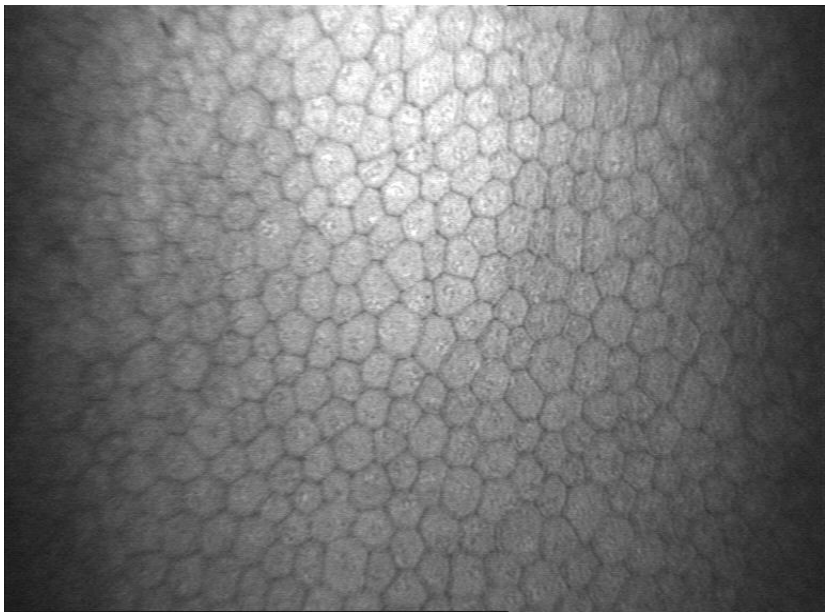

Figure 5.1: A representative image of cornea endothelium obtained with the ConfoScan 4 confocal microscope (Nidek Technologies, Italy).

The endothelial cells are polygonal with four to eight borders, mostly hexagonal. They have a diameter of about 22 μm and a surface area of about 250 μm^2. Ideal endothelia are made of regular hexagonal cells of similar area, but this regular tessellation is affected by age and pathologies. Corneal endothelial cells do not

reproduce, therefore pathologies affecting the endothelium permanently damage the layer. Death of corneal endothelial cells is compensated by enlargement and migration of neighboring cells, which change the regular hexagonal pattern. The deviation of the cell field from the regular hexagonal pattern is therefore an indicator of the corneal damage. A quantitative analysis may provide information on cell density, polymegathism (distribution of cell sizes), and pleomorphism (distribution of number of cell sides). This information could be easily extracted if the cell contours are identified in the image, and several prototype systems for the automatic analysis of corneal endothelium based on the identification of cell contours have been proposed, [44, 45, 46, 47, 48, 49]. Unfortunately, due to cornea anatomy and specific features of image acquisition, images are often blurred and noisy, so that contour recognition is rather difficult and these systems often require operator interaction to correct errors. This manual processing is obviously very tedious and time consuming, and therefore the availability of an automatic system for image processing would be an immense aid.

27 images of corneal endothelium were made available by Nidek Technologies from their own image database. They were acquired with the Confoscan4 confocal microscope (Nidek Technologies, Italy) at 40X magnification. Each image covers a field of 460x350 μm, and was saved as a monochrome 768x576 pixel digital image.

5.2 Illumination and contrast correction

The images from corneal microscopes, especially confocal ones, usually present a non-uniform illumination (Figure 5.1). In order to cope with this and at the same time reduce the amount of noise in the image, a parabolic correction and a band-pass filter are applied to the observed images. The parabolic correction compensates the illumination drift by fitting it with a parabolic (second order) function and then subtracting it from the image, both horizontally and vertically. The band-pass filter adopted has cut-off frequencies of $0.02f_c$ and $0.2f_c$ where f_c is the spatial sampling frequency of the image. After parabolic and band-pass pre-processing, the image has a uniform illumination (Figure 5.2). Contrast, especially the one between dark cell boundaries and light cell bodies, is generally very low in this kind of images. Local contrast is enhanced by means of a sigmoid point transformation, centered on the image mean value and applied to the entire image.

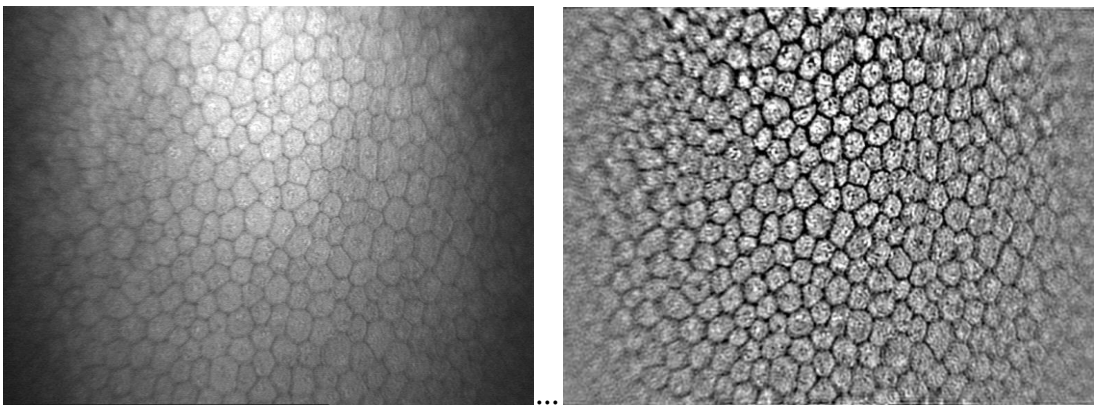

Figure 5.2: Original image and pre-processed version

5.3 Segmentation

The segmentation into cell bodies and cell boundaries is achieved by a multi-layer feed-forward artificial neural network (ANN), with local shift invariant interconnections to meet the shift-invariant processing [50, 51].
Each pixel of the image is considered and its 121 (11x11 pixels) adjacent pixels are used to extract 7 features and to classify the pixel into 8 classes. The features and the number of classes are chosen according to the Fisher linear discriminant analysis method (see the following paragraph). The 8 classes are:

- cell body;
- vertical border;
- horizontal border;
- oblique border;
- border with angle towards left;
- border with angle towards right;
- border with angle towards up;
- border with angle towards down.

Finally, each pixel is classified into cell body (the first class) or cell boundaries (one of the other 7 classes).
The adopted network is composed of 1 input, 2 hidden layers, and 1 output.

5.3.1 Features selection

For each pixel of the image, a small region, centered on the pixel, is considered. The region has dimension 11x11 pixels (121 neighbors), and the 121 pixel intensity values are used to extract the features used by the neural network. There are several reasons that suggest to keep as low as possible the number of features with which to classify the candidate pixel. The first is computational complexity. Another is that the increase in complexity in computing a larger number of features is not always matched by an increase in discriminatory power, because of the possible redundancy and correlation among features. The most important reasons lie however in the generalization power of a classifier. Since the number of features can be considered as the number of free parameters of the classifier, the smaller the ratio between this number and the cardinality of the training set, the better the performance on the training set but the less robust the classifier.
A common method to select the most significant features is the Fisher linear discriminant analysis method [LDA], which ensures optimal linear separation between features by seeking the direction that minimizes interclass cross-variance. LDA is a method for linearly mapping the high dimensional characteristics vector in a lower dimensional space, which maximize the separation between classes, supposing their distribution normal. LDA is based on the maximization of a function $J(.)$ that is an indicator of the class separation. Given N samples, M classes and a $1 \times m$ vector w of features, the function J considered is:

$$J(w) = \frac{w^T S_B w}{w^T S_W w}$$

where S_B is the "between classes scatter matrix" and S_W is the "within classes scatter matrix". The definitions of the scatter matrices are:

$$S_B = \sum_{i=1}^{M} N_i (\mu_i - \mu)(\mu_i - \mu)^T$$

$$S_W = \sum_{i=1}^{M} \sum_{j \in i} (x_j - \mu_i)(x_j - \mu_i)^T$$

where ^{T} denotes the transpose, N_i is the number of samples in the class i, μ_i is the mean of samples in the class i and μ is the mean of all samples:

$$\sum_{i=1}^{M} N_i = N \qquad \mu_i = \frac{1}{N_i} \sum_{j \in i} x_j \qquad \mu = \frac{1}{N} \sum_{i=1}^{M} x_i$$

A linear transformation mapping the original m dimensional features space into a new (M-1) dimensional space can therefore yield the same value for J while obtaining a lower dimensionality. A vector that maximizes $J(.)$ must satisfy:

$$S_B w = \lambda S_W w$$

This problem could be viewed as an eigenvalue problem: the matrix describing the linear transformation is in fact the matrix having on its columns the $(M-1)$ non trivial eigenvectors of $(S_W)^{-1} S_B$.
In endothelial image, the non trivial eigenvectors are 7. Thus, the number of features used in the artificial neural network is 7 $(M-1)$ and the number of classes has to be 8 (M).

5.3.2 Artificial neural network training process

The training set is composed by 5 ROIs (120x120 pixel), which were selected in 5 different images of the dataset (Figure 5.3). In order to find cell boundaries, a manual segmentation was performed. These is a first classification: cell bodies and cell boundaries. Then, cell boundaries are manually classified into 7 classes: vertical, horizontal and oblique size, and angle towards left, right, up and down. Finally, 8 classes are used (cell body + 7 cell boundary types). Manually segmented images are the target images (Figure 5.4).

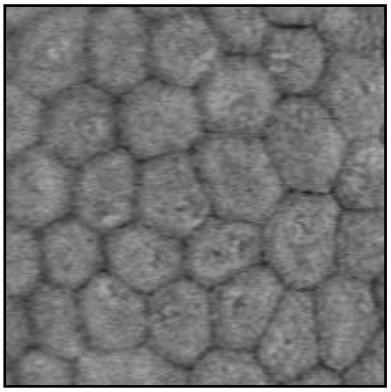

Figure 5.3: training input image (120x120 pixels)

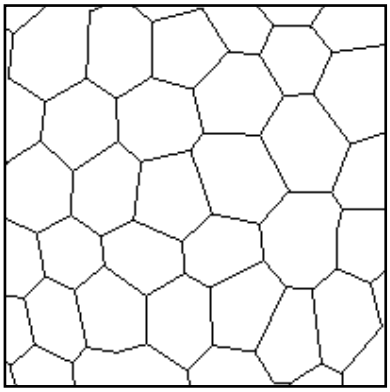

Figure 5.4: training target image (cell bodies and cell boundaries)

The ANN training process is the classical backpropagation technique. Input images (5 ROIs) and the corresponding target images are used to train the network until it can classify input images in an appropriate way as defined by target images. Standard backpropagation is a gradient descent algorithm, in which the network weights are moved along the negative of the gradient of the performance function. The simplest implementation of backpropagation learning updates the network weights and biases in the direction in which the performance function decreases most rapidly, the negative of the gradient. One iteration of this algorithm can be written:

$$x_{k+1} = x_k - \alpha_k g_k$$

where x_k is a vector of current weights and biases, g_k is the current gradient, and α_k is the learning rate. This gradient descent algorithm can be implemented in incremental mode, using the Newton's method. The basic step of Newton's method is:

$$x_{k+1} = x_k - A_k^{-1} g_k$$

Where A_k^{-1} is the Hessian matrix (second derivatives) of the performance index at the current values of the weights and biases. Newton's method often converges fast, but, unfortunately, it is complex and expensive to compute the Hessian matrix for feed-forward neural networks. To solve this problem, the Levenberg-Marquardt algorithm is used. It was designed to approach second-order training speed without having to compute the Hessian matrix:

$$H = J^T J$$

and the gradient can be computed as

$$g = J^T e$$

where J is the Jacobian matrix that contains first derivatives of the network errors with respect to the weights and biases, and e is a vector of network errors. The Jacobian matrix can be computed through a standard backpropagation technique that is much less complex than computing the Hessian matrix. The Levenberg-Marquardt

algorithm uses this approximation to the Hessian matrix in the following Newton-like update:

$$x_{k+1} = x_k - \left[J^T J + \mu I\right]^{-1} J^T e$$

When the scalar μ is zero, this is just Newton's method, using the approximate Hessian matrix. When μ is large, this becomes gradient descent with a small step size. Newton's method is faster and more accurate near an error minimum, so the aim is to shift toward Newton's method as quickly as possible. Thus, μ is decreased after each successful step (reduction in performance function) and is increased only when a tentative step would increase the performance function. In this way, the performance function is always reduced at each iteration of the algorithm. The result is shown in the following figures:

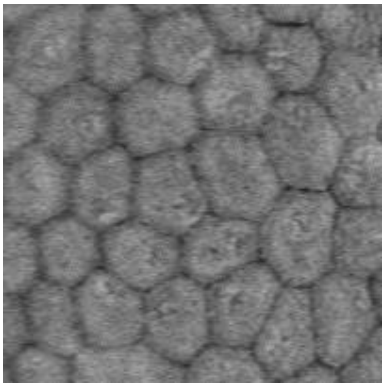

Figure 5.5: training input image (120x120 pixels)

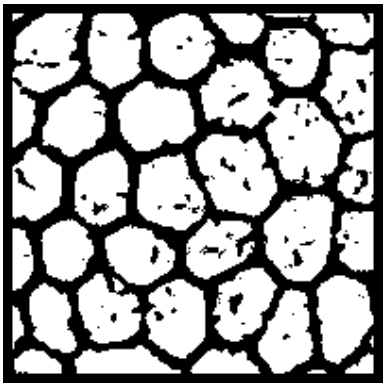

Figure 5.6: ANN output. It is the automatically segmented image (cell bodies and cell boundaries)

5.4 Automatic ROI selection

In order to exclude, from further analysis, the dark and unfocused areas in the peripheral regions of the image, an image ROI is automatically selected using a procedure that combine entropy and power spectral density.

5.4.1 Entropy

The concept of entropy has been widely used to measure the information content of an image [52]. The entropy of an image X with possible pixel intensity values $\{x_1,\ldots,x_N\}$ can be define as:

$$H(X) = E[I(X)]$$

Where *E* is the *expected value function*, and *I(X)* is the information content or *self-information* of *X*. Entropy can explicitly be written as:

$$H(X) = \sum_{i=1}^{N} p(x_i) I(x_i) = -\sum_{i=1}^{N} p(x_i) \log(p(x_i))$$

Where *p* denotes the *probability mass function*, and is derived for each image from pixel intensity values.

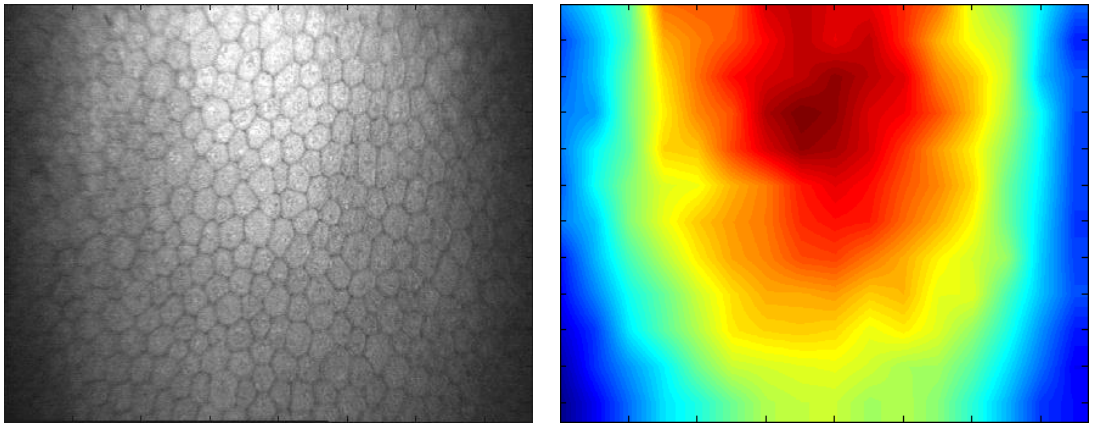

Figure 5.7: Original image and its entropy.

5.4.2 Power Spectral Density

The power spectral density (PSD) of an image is defined as the squared modulus of the Fourier transform of the image. It is estimated by dividing the image into successive blocks, and averaging squared-magnitude DFT (Discrete Fourier Transform) of the blocks:

$$PSD = \frac{1}{M} \sum_{m=0}^{M-1} \left| DFT(x_m) \right|^2$$

Where *M* denotes the number of blocks, and x_m are the elements of the m^{th} block.

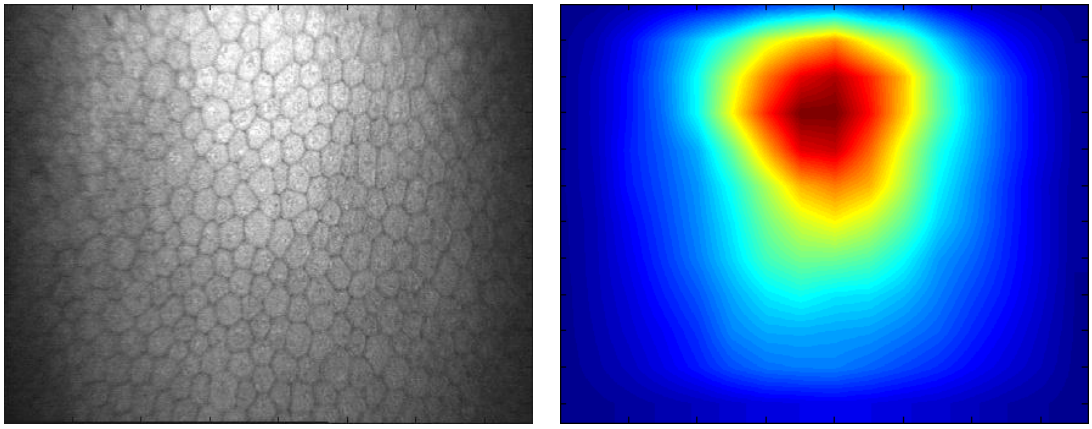

Figure 5.8: Original image and its power spectral density.

5.4.3 Entropy and Power Spectral Density interpolation

Entropy and Power Spectral Density are linearly combined in the image *I* (figure 5.9) as follows:

$$I = w_1 \cdot H + w_2 \cdot PSD$$

Where *H* is the entropy, *PSD* is the power spectral density, *w1* and *w2* are weights. The values of the weights are established using the Fisher method, maximizing the function:

$$J(w) = \frac{(m_2 - m_1)^2}{s_1^2 + s_2^2}$$

Where *m* represents the mean, s^2 represents the variance, and the subscripts denote the two classes (focused and unfocused) manually determined in 5 training images. In order to select the ROI, a threshold is applied to the image *I*. The threshold was empirically determined. Only the part of the ANN output inside the selected ROI is considered for analysis.

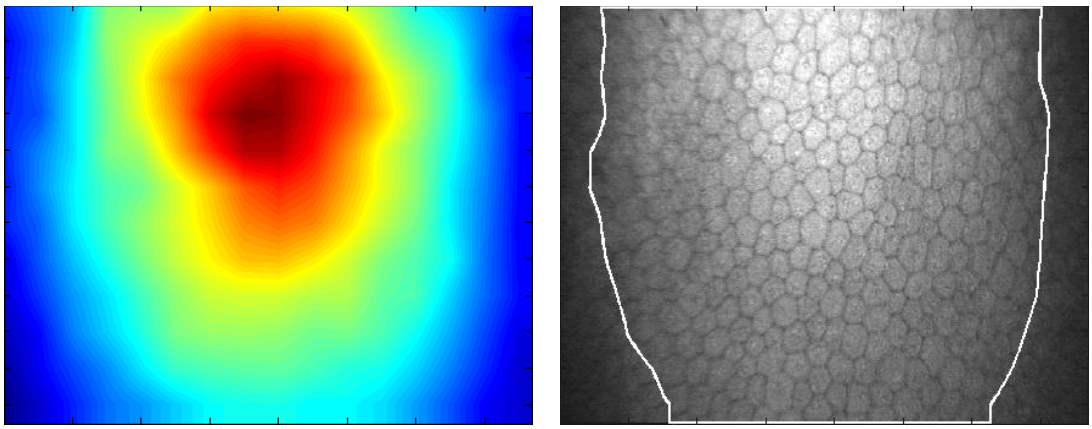

Figure 5.9: Entropy and PSD liner combination (left) and ROI selection (right).

5.5 Post-processing

The ANN binary output (see Figure 5.6 for example) is then processed with morphological operators to obtain the skeleton of the cell boundaries.
The lack of significant differences in gray levels between cell boundaries and cell bodies prevented this pixel value based processing from reaching an overall acceptable segmentation, i.e. some parts of boundaries are classified as cell bodies (missing boundaries) and some cell bodies are partially classified as boundaries (false boundaries). Further processing is therefore needed to correct these problems.

5.5.1 Contour completion

A first correction is performed by connecting pairs of skeleton floating stumps that clearly match in direction and are not too far apart from each other (Figure 5.10). This process may also introduce new false boundaries, but this apparent drawback is dealt with by the next steps of the post-correction ("expert correction" [46]).

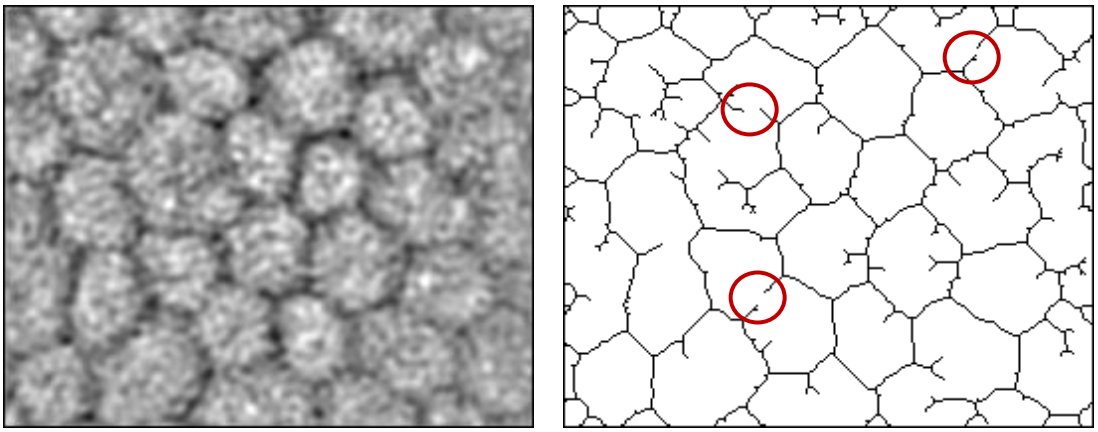

Figure 5.10: Connections of skeleton floating stumps.

Cell body contours are extracted from the image using morphological operators. For every cell identified, a set of features is evaluated, such as mean radius, standard deviation of radius, standard deviation of relative radius (radius/mean radius), aspect ratio (ratio of the two main diagonals). Trying to improve an overall 'cell score', based on the values of these features, some attempts are made to fuse small adjacent cells or to split large cells. This is done according to a general paradigm of trying to reach uniformity of features among the cells: any operation (splitting or fusion) is accepted if it improves the uniformity of the features. In computing the score, features with a high variability (i.e. high standard deviation) are weighted less than features that present a uniform pattern (i.e. low standard deviation).
At first, cell bodies presenting a particular combination of size (bodies significantly larger than the median value) and aspect ratio (significantly higher than the median) are taken into consideration for splitting. For every floating stump inside the cell body, extension along its direction and along the direction orthogonal to the cell

main diagonal are considered. Decision of whether the splitting has to be accepted or rejected, and which of the two possible directions has to be used for splitting, is taken trying to maximize the improvement in the 'cell score'. In a similar way, every small cell is considered for potential fusion with the neighboring cells. The best fusion, if any, with respect to the 'cell score' is actually performed. This iterative process ends when no splitting or fusion operation improves the present configuration.

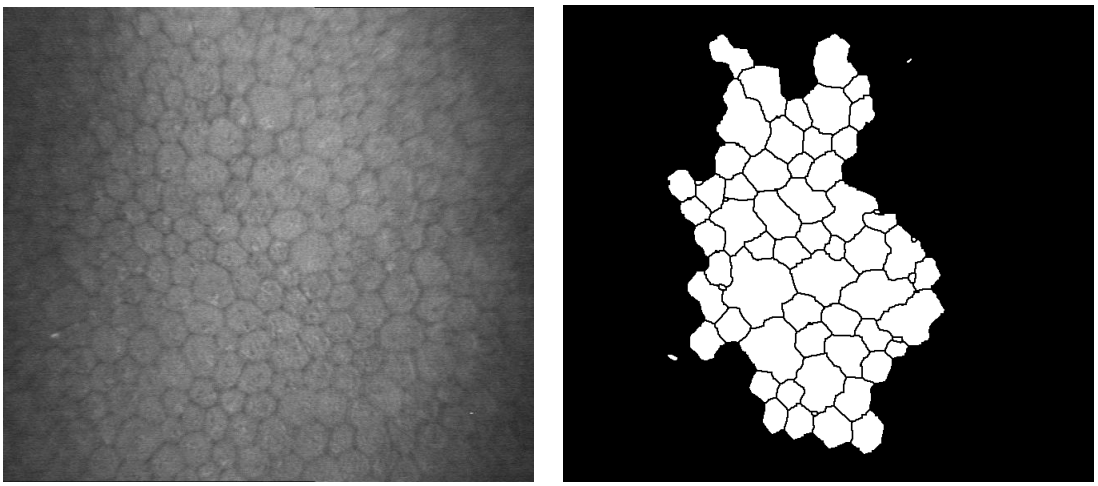

Figure 5.11: Selected ROI and segmented image after contour completion.

5.5.2 Split and merge

A module is added to split and merge cells with unrealistic shape and area. In order to merge cells with small area, for each cells, boundary pixels are considered and the portion of the boundary with the highest intensity is recognized. The cell adjacent to this portion is merged with the small cell, but the fusion is accepted only if the resulting cell has uniform features, otherwise the fusion is rejected and another adjacent cell, if any, is considered (Figure 5.12).

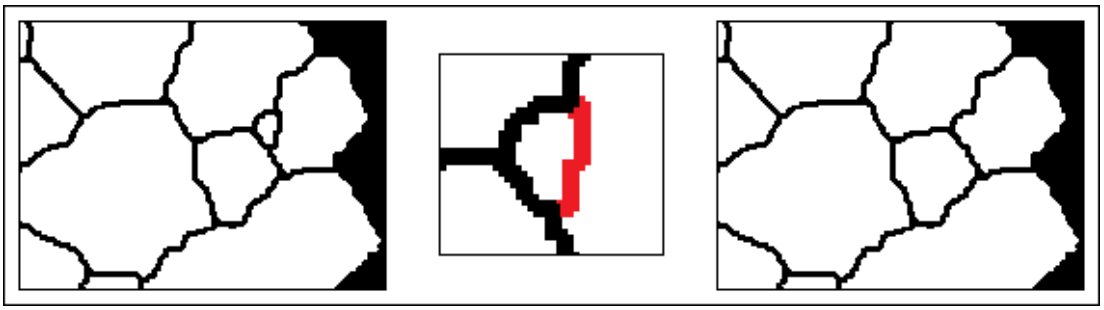

Figure 5.12: Merge cells.

As regards cells with high area, the contour of each cell is analyzed and concave portions are recognized. The cell is split by linking two concave portions, and this partition is accepted only if the new cells have uniform features and if the new side corresponds to dark pixels in the original image (Figure 5.13). If this method fails,

cell body intensity is considered and dark regions are recognized using a threshold. The next step is link these regions. Again, the partition is accepted only if the new cells have uniform features and if the new sides correspond to dark pixels in the original image (Figure 5.14). Merge and split methods are iteratively performed until no splitting or fusion operation improves the present segmentation.

Figure 5.13: Split cells (method 1).

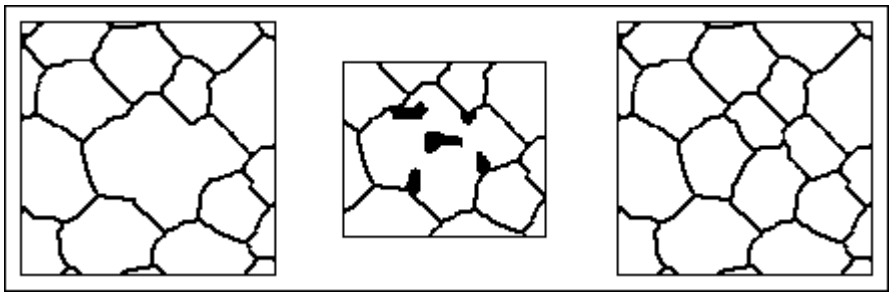

Figure 5.14: Split cells (method 2).

5.6 Performance evaluation

The proposed algorithm was evaluated on the dataset composed of 27 images (see paragraph 5.1).

On average, 97,4% of the endothelial cells actually found by the automatic procedure are correctly recognized (Table 5.1): the mean number of found cells per image is 142,7 and of these, on average, 138,9 cells per image are correctly recognized. The remaining cells do not correspond to a real cell in the image. A representative example of the result obtained is shown in Figure 5.15.

Table 5.1: Results obtained using a dataset of 27 images.

Number of cells	Recognized cells	Correctly recognized	diff	%
Average	142,7	138,9	3,81	97,4%
Std Dev	24,9	24,2	3,06	2,1%
Min	176	70	0	92,0%
Max	70	172	11	100,0%

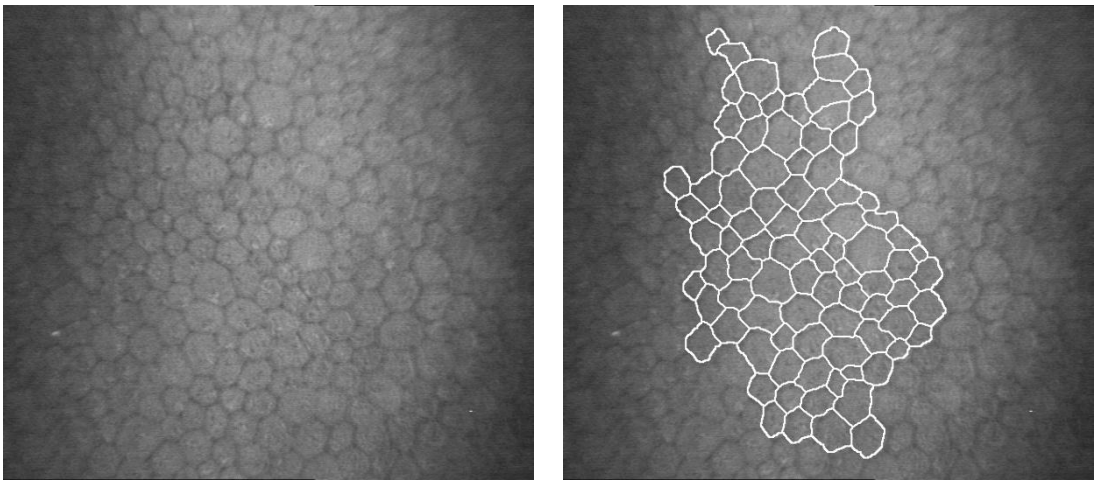

Figure 5.15: Automatic cell contour detection.

In order to evaluate the performance of the algorithm, manual segmentation was also performed on the same images. For each image of the dataset, clinical parameters are computed starting from both automatic segmented images and manual segmented images. The clinical parameters are:

- density (cells/mm^2);
- pleomorphism (percentage of hexagonal cells);
- polymegathism (coefficient of variation in cell area).

The results of automatic estimation of the cellular density are reported in Table 5.2. The clinical indexes are very different in the various images, ranging, as regards density, from 1598 to 3523 cells/mm^2 by manual method, and from 38,6 to 72,7 and from 32,2 to 40,7 as regards pleomorphism and polymegathism. They are in good agreement with measurements done by the manual counting method (average difference: -2%). Good agreement is also obtained for pleomorphism (average difference: -1%) and polymegathism (average difference: 0%). Their results are reported in Table 5.3 and Table 5.4 respectively.
Considering the absolute value of the indexes in each image, the percent differences between automatic density, polymegathism, pleomorphism and the corresponding manual ones are, on average, -3%, 9%, 8% respectively.

Table 5.2: Statistics of estimated density in the 27 images.

Density (cells/µm^2)	**manual method**	**automatic method**	**diff**	**%**	**abs**	**%**
Average	2793	2727	-66	-2%	95	3%
Std Dev	453	400	102	3%	74	2%
Min	1598	1633	-341	-10%	5	0%
Max	3523	3396	183	7%	341	10%

Table 5.3: Statistics of estimated pleomorphism (percentage of hexagonal cells) in the 27 images.

pleomorphism	manual method	automatic method	diff	%	abs	%
Average	59,1	58,3	-0,7	-1%	5	9%
Std Dev	8,2	8,8	7,0	12%	5	8%
Min	38,6	39,7	-14,1	-21%	0	0%
Max	72,7	76,3	18,3	32%	18	32%

Table 5.4: Statistics of estimated polymegathism (standard deviation / average of cell areas) in the 27 images.

polymegathism	manual method	automatic method	diff	%	abs	%
Average	30,5	30,3	-0,3	0%	2,4	8%
Std Dev	4,9	4,3	3,1	10%	1,9	6%
Min	23,2	24,1	-5,2	-16%	0,1	0%
Max	40,7	39,6	6,7	22%	6,7	22%

Figure 5.16, Figure 5.18, and Figure 5.20 show the scatter plots of manually versus automatically estimated cell density, pleomorphism and polymegathism. From this graphic representation of the results, the correlation between the automatic and manual method can be appreciated and quantitatively described by the correlation coefficient, which was 0,97 for density and 0,78 and 0,66 for pleomorphism and polymegathism, respectively. Pleomorphism and polymegathism are very sensitive to segmentation errors.

In Figure 5.17, Figure 5.19, and Figure 5.21 there are the corresponding Bland-Altman plots, showing difference between automatic and manual methods for density, pleomorphism and polymegathism. Average difference is -65,6 μm for density and -0,7 and -0,3 for pleomorphism and polymegathism, respectively. The dashed lines indicate the average difference and the 95% limits of agreement: it is -266 μm ÷ 134 μm for density, -14,4 ÷ 12,9 for pleomorphism, and -6,3 ÷ 5,8 for polymegathism.

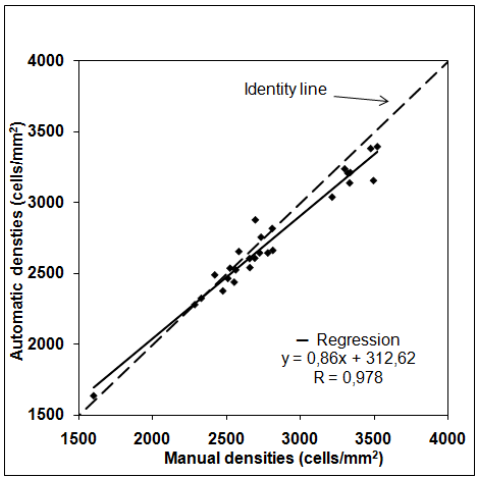

Figure 5.16: Scatter-plot of cell density from manual vs. automatic method.

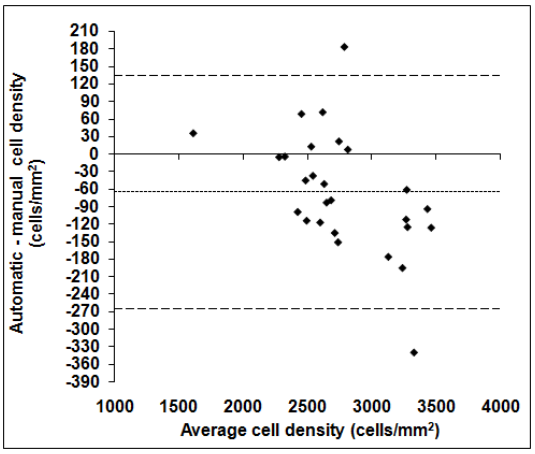

Figure 5.17: Bland-Altman plot for cell density from manual and automatic methods. It displays the difference vs. average for each pair of manual and automatic density, with three lines indicating the mean difference (dotted line) and the 95% limits of agreement (dashed lines).

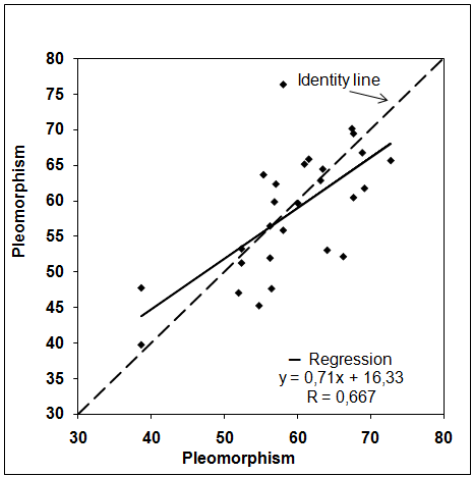

Figure 5.18: Scatter-plot of pleomorphism from manual vs. automatic method.

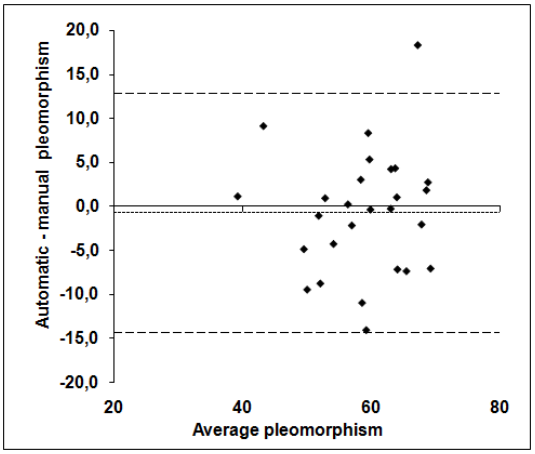

Figure 5.19: Bland-Altman plot for pleomorphism from manual and automatic methods. It displays the difference vs. average for each pair of manual and automatic pleomorphism, with three lines indicating the mean difference (dotted line) and the 95% limits of agreement (dashed lines).

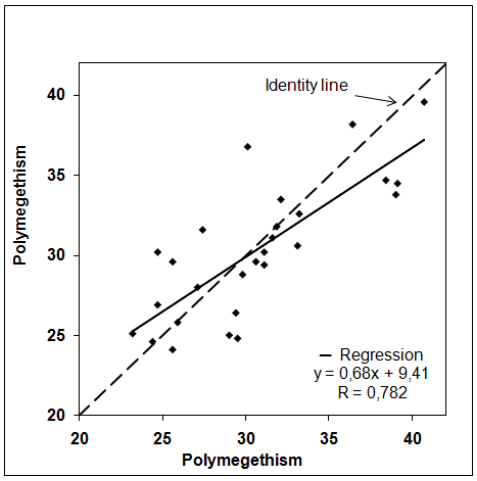

Figure 5.20: Scatter-plot of polymegathism from manual vs. automatic method.

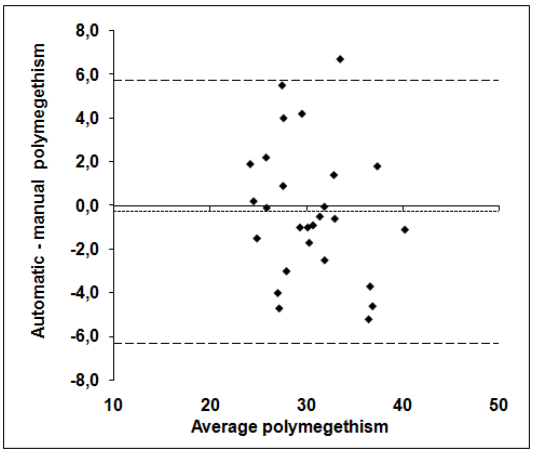

Figure 5.21: Bland-Altman plot for polymegathism from manual and automatic methods. It displays the difference vs. average for each pair of manual and automatic polymegathism, with three lines indicating the mean difference (dotted line) and the 95% limits of agreement (dashed lines).

Chapter 6

Conclusions

6.1 Achieving the Objectives

The aim of this thesis was to develop a system for the automatic processing and analysis of confocal images of the various layers of the cornea. This has been achieved by developing the system in a modular way, with every module solving a well defined task. This approach may lack the global perspective that a human grader has in evaluating the state of a cornea, but it is useful in breaking down a very hard problem into simpler ones that are computationally tractable.

Several aspects of corneal image processing and automatic estimation of different clinical parameters have been addressed, in order to give to the ophthalmologist the most comprehensive view of the cornea state. The main achievements will be summarized in the following sections.

6.1.1 Nerves tracing

A lot of clinical parameters indicating cornea state of health are related to morphological features of the nerve fibers. In order to detect and quantitatively describe these parameters, the layout of the nerves contained in the image has to be extracted.

The point was solved by using a tracing technique. First, images are normalized and enhanced in luminosity and contrast. Due to the presence of keratocytes and to the local decrease in image contrast, a tracing procedure that starts from different points along a nerve is required. This is achieved by using a sparse approach, in which a set of widespread starting points within an image is identified. Then, starting from each point, the tracing module detects the nerve direction and then moves along a nerve by drawing successive segments perpendicular to the nerve direction (cross section). Pixel on each cross section are analyzed, with a local clustering algorithm, to classify them into “nerve” and “background” pixels. The tracing procedure includes Gabor filtering to enhance nerve visibility and the “bubble analysis”. This analyzes a set of concentric rings around a point, in order to gather information on the position of nerves in the neighborhood of the central points with a larger perspective than that of the tracking step. After nerve segments are recognized, a post-processing procedure removes false recognitions and links sparse segments.

A prototype of the algorithm was implemented in commercial software language (Matlab; The MathWorks, Natick, MA) and run on a personal computer.

The algorithm was evaluated on 2 datasets. The first dataset is composed by 90 images from normal and non-normal subjects. In this dataset, the correlation coefficient between the automatic and manual method is 0,94 for all images and 0,95 and 0,86 for normal and non normal-images, respectively. On average, more than 80% of the nerve actually present in an image are correctly recognized, and fewer than 7% of false recognitions are present in the nerves detected by the automatic procedure with slightly more correct recognitions but also more false recognitions in non-normal images. The second dataset is composed by 80 images obtained from an independent source, and the correlation coefficient between the automatic and manual method for these images is 0,89.

6.1.2 3D reconstruction and keratocyte density estimation

The corneal stroma is populated by keratocytes, whose nuclei are visible in confocal microscopy. Several investigators have examined changes in morphology and density of these cells. In this thesis was presented an algorithm that is able to visualize them and to automatically estimate their density starting from a sequence of images.

All the images in each sequence were registered to compensate for possible x-y shifts, in order to obtain a 3D stack of z-aligned images. If data are missing, we reconstruct them by taking lines from adjacent images and interpolating them. After reconstruction, it is possible to display and analyze corneal structures in the 3D volume and obtain slices in the x, y, or z direction. After image enhancement and ROI selection, a custom segmentation procedure, based on a modified Otsu technique, was applied to each image to detect 2D contour and center of keratocytes. Only images from the central part of the sequence, i.e., containing no epithelial nor endothelial cells, were used. A clustering step was then applied to all the images of the stack, so as to identify the 3D contour and center of keratocytes. Each stack of images was then partitioned into 5 adjacent layers: anterior stroma (0%-10% of stromal depth); anterior (11%-33%), central (34%-66%) and posterior (67%-90%) mid stroma; and posterior stroma (91%-100%). Keratocytes centers were counted in each layer, to eventually estimate their volumetric density. The entire procedure is fully automatic and requires no user input. Manual detection of keratocytes on each 2D image and then on the 3D stacks of images was also performed.

The prototype was implemented using the programming languages Matlab, C++ and OpenGL (Open Graphics Libraries, developed by Silicon Graphics Inc), and run on a personal computer.

The algorithm was evaluated on 3 sequences of normal subject. 101 stroma images were analyzed in subject nr. 1, 68 in nr. 2, and 103 in nr. 3. The percent differences between automatic keratocyte densities and the corresponding manual ones were compared in the 5 corneal layers. In this limited data set of normal images, very good average automatic vs. manual differences were obtained (range: -2.9%; 6.5%).

6.1.3 Cell contour detection

In-vivo microscopy of corneal endothelium is a technique routinely adopted in ophthalmic investigation. The main features to be extracted are cell density and morphology.

The algorithm proposed in this thesis detects cell contours and computes density, polymegathism, pleomorphism. It is composed of a first segmentation module, based on a neural network structure with two-dimensional inputs and outputs, whose neuron weights are numerical filters specifically designed for a border extraction problem. In order to exclude the dark and unfocused peripheral area of the image, a ROI is automatically selected using a procedure based on entropy and power spectral density. However, grey-level information alone is not sufficient to correctly discriminate between cell bodies and cell boundaries. To cope with the wrong results still present in the segmented image (missing contours or false contours), a post-processing procedure has been developed based on an automatic, multi-step approach, which includes missing contour recovery and tentative merging and splitting of cell bodies.

The prototype of the algorithm was implemented using the programming languages Matlab and C++, and run on a personal computer.

The proposed algorithm was evaluated on a dataset composed by 27 images. On average, 97,4% of the endothelial cells actually found by the automatic procedure are correctly recognized. The percent differences between automatic density, polymegathism, pleomorphism and the corresponding manual ones were, on average, -2%, -1%, 0% respectively (3%, 9%, 8% considering, in each image, the absolute value of the indexes). The correlation coefficient between the automatic and manual method is 0,97 for density and 0,78 and 0,66 for pleomorphism and polymegathism, respectively.

6.2 The way ahead

The algorithms presented in this thesis make it possible to conceive a tool to be used for the automatic analyses of the cornea. It allows to obtain a quantitative and reproducible description of the whole cornea and quantitative details of the single structures. It is composed by three algorithm that analyze three different layers: sub-basal layer, stroma and endothelium. Improvements can be introduced in each algorithm, as describe in the following paragraph.

To the author’s knowledge, the system presented here is the only ever proposed for the automatic detection of the corneal sub-basal nerve structures. With its application, important clinical parameters such as total length of nerves in the image, nerve density, nerve tortuosity, could be readily derived in an easy, quantitative and reproducible way. Work is in progress to develop additional computer programs to derive and evaluate the above mentioned clinical parameters. As regards processing time, in order to extract nerve fibers, the prototype Matlab computer program required approximately 1 minute per image. Implementation of the algorithm with a more efficient computer language, e.g. C++, will reduce the analysis time to few seconds per image.

In order to obtain a better visualization of corneal structures in the volume, image restoration techniques, such as blind deconvolution, can be applied. An extensive evaluation of the proposed algorithm will be performed in a larger set of confocal sequences, including also pathological subjects. Work is in progress to improve the segmentation procedure to better detect 2D contour and center of keratocytes, and to estimate their density.

The algorithm for endothelial cell contour detection is still under development in order to add new features that can better deal with pathological situations (very large or very small cell bodies) and avoid incorrect fusion or splitting. These latter are sometimes triggered in highly corrupted areas of the original image, when the system tries to achieve an acceptable cell bodies pattern.

It is quite important to compare the methods and the results presented in this thesis to those determined by histology or other accepted methods. It is also crucial to compare them with results obtained using other confocal microscopes: the estimated density of nerves and cells also depends somewhat on the instrument used to record images [55].

Finally, there is the need to enlarge the dataset and use as many independent samples as possible to represent the images that will be examined in the future, in order to make the algorithms useful for normal and non-normal corneas.

Bibliography

[1] Mastropasqua L, Nubile M, "Confocal Microscopy of the Cornea" SLACK Incorporated, 2002, pp 1-16.

[2] Jalbert I, Stapleton F, Papas E, Sweeney DF, Coroneo M, *"In vivo confocal microscopy of the human cornea"* British Journal of Ophthalmology. 2003; vol 87: pp 225-236.

[3] Erie JC, McLaren JW, Hodge DO, Bourne WM, *"The effect of age on the corneal subbasal nerve plexus"* Cornea. 2005; vol 24: pp 705–709.

[4] Patel S, McLaren JW, Hodge DO, Bourne WM, *"Confocal microscopy in vivo in corneas of long-term contact lens wearers"* Investigative Ophthalmology & Visual Science. 2002; vol 43: 995–1003.

[5] Moilanen JAO, Vesaluoma MH, Müller LM, Tervo TMT, *"Long-term corneal morphology after PRK by in vivo confocal microscopy"* Investigative Ophthalmology & Visual Science. 2003; vol 44: pp 1064–1069..

[6] Erie JC, McLaren JW, Hodge DO, Bourne WM, "*Recovery of Corneal Subbasal Nerve Density after PRK and LASIK*" American Journal of Ophthalmology. 2005; vol 140: pp 1059–1064.

[7] Niederer RL, Perumal D, Sherwin T, McGhee CNJ, *"Corneal innervation and cellular changes after corneal transplantation: an in vivo confocal microscopy study"* Investigative Ophthalmology & Visual Science. 2007; vol 48: pp 621–626.

[8] Benitez del Castillo MJ, Wasfy MAS, Fernandez C, Garcia-Sanchez J, *"An in vivo confocal masked study on corneal epithelium and subbasal serves in patients with dry eye"* Investigative Ophthalmology & Visual Science. 2004; vol 45: pp 3030–3035.

[9] Tuominen ISJ, Konttinen YT, Vesaluoma MH, Moilanen JAO, Helintö M, Tervo TMT,. *"Corneal innervation and morphology in primary Sjögren's syndrome"* Investigative Ophthalmology & Visual Science. 2003; vol 44: pp 2545-2549.

[10] Patel DV, McGhee CNJ, *"Mapping the Corneal Sub-basal Nerve Plexus in Keratoconus by In Vivo Laser Scanning Confocal Microscopy"* Investigative Ophthalmology & Visual Science. 2006; vol 47: pp 1348–1351.

[11] Simo Mannion L, Tromans C, O'Donnel C, *"An evaluation of corneal nerve morphology and function on moderate keratoconus"* Contact Lens Anterior Eye, 2005; vol 28: pp 185–192.

[12] Rosenberg ME, Tervo TMT, Müller LJ, Moilanen JAO, Vesaluoma MH, *"In vivo confocal microscopy after herpes keratitis"* Cornea. 2002; vol 21: pp 265–269.

[13] Kallinikos P, Berhanu M, O'Donnel C, Boulton A, Efron N, Malik R, *"Corneal nerve tortuosity in diabetic patients with neuropathy"* Investigative Ophthalmology & Visual Science. 2004; vol 45: pp 418–422.

[14] Li J, Jester JV, Cavanagh HD, Black TD, Petroll WM, *"On line 3-dimensional confocal imaging in vivo"* Investigative Ophthalmology & Visual Science. 2000; vol 41: pp. 2945–2953.

[15] Stachs O, Zhivov A, Kraak R, Stave J, Guthoff,R, *"In vivo threedimensional confocal laser scanning microscopy of the epithelial nerve structure in the human cornea"* Graefes Arch Clin Exp Ophtalmol, 2006.

[16] Guthoff RF, Wienss H, Hahnel C, Wree A, *"Epithelial innervations of human cornea: a three-dimensional study using confocal laser scanning fluorescene microscopy"* Cornea, July 2005, vol. 24, nr 5, pp. 608–613.

[17] Berlau J, Becker HH, Stave J, Oriwol C, Guthoff RF, *"Depth and age-dependent distribution of keratocytes in healthy human corneas"* Journal of Cataract & Refractive Surgery 2002, vol 28: pp 611-616.

[18] Patel SW, McLaren JW, Hodge DO, Bourne WM *"Confocal microscopy in vivo in corneas of long-term contact lens wareers"* Investigative Ophthalmology & Visual Science. 2002; vol 43; nr 4: pp 689-695.

[19] Ku JYF, Niederer R, Patel DV,Sherwin T, McGhee CNJ, *"Laser Scanning In Vivo Confocal Analysis of Keratocyte Density in Keratoconus"* Ophthalmology 2008; vol 115, nr 5, pp 845-850.

[20] Erie JC, McLaren JW, Hodge DO, Bourne WM *"Long-term corneal keratocyte deficits after photorefractive keratectomy and laser in situ keratomileusis"* American Ophthalmological Society. 2005; vol 103: pp 56-68.

[21] Ivarsen A, Laurberg T, Møller-Pedersen T, *"Role of Keratocyte Loss on Corneal Wound Repair after LASIK"* Investigative Ophthalmology & Visual Science. 2004; vol 45; nr 10: pp 3499-3506.

[22] Bourne WM, *"Cellular changes in transplanted human corneas"* Cornea, 2001; vol 20; nr 6: pp 560-569.

[23] Patel SV, McLaren JW, Hodge DO, Bourne1 WM *"Normal Human Keratocyte Density and Corneal Thickness Measurement by Using Confocal Microscopy In Vivo"* Investigative Ophthalmology & Visual Science. 2001; vol 42; nr 2: pp 333-339.

[24] Hahnel C, Somodi S, Weiss DG, Guthoff RF, *"The keratocyte network of human cornea: a three-dimensional study using confocal laser scanning fluorescene microscopy"* Cornea, 2000, vol. 19, nr 2, pp. 185–193.

[25] Nassiri N, Rahnavardi M, Rahmani L, *"A comparison of corneal endothelial cell changes after 1-site and 2-site phacotrabeculectomy"* Cornea, Sep 2008, vol. 27, nr 8, pp. 889-894.

[26] Alsuhaibani AH, Al-Rajhi AA, Al-Motowa SM, Wagoner MD, *"Corneal endothelial cell density and morphology after acute hydrops in keratoconus"* Cornea, Jun 2008, vol. 27, nr 5, pp. 535-538.

[27] Lehto I, Ruusuvaara P, Setälä K, *"Corneal endothelium in pigmentary glaucoma and pigment dispersion syndrome"* Acta Ophthalmologica (Copenh), Dec 1990, vol. 68, nr 6, pp. 703-709.

[28] Grisan E, Pesce A, Giani A, Foracchia M, Ruggeri A, *"A new tracking system for the robust extraction of retinal vessel structure"* Proc. 26th Annual International Conference of IEEE-EMBS, New York, 2004, pp. 1620–1623.

[29] Foracchia M, Grisan E, Ruggeri A. *"Luminosity and contrast normalization in retinal images"* Medical Image Analysis. 2005; vol 9: pp 179–190.

[30] Grisan E, *"Automatic Analysis of Retinal Images: Retinopathy Detection and Grading"*, PhD Thesis, 2005.

[31] Bezdek JC, "*Pattern recognition with fuzzy objective function algorithms"* Plenum. New York, 1981.

[32] Giani A, Grisan E, DeLuca M, Ruggeri A, "*Detecting false vessel recognitions in retinal fundus analysis*" Proc. 26th Annual International Conference of IEEE-EMBS, New York, 2004, pp. 4449–4452.

[33] Gonzalez RC, Woods RE, "*Digital Image Processing*" 2nd ed. Upper Saddle River, NJ: Prentice Hall, 2002.

[34] www.bioimlab.dei.unipd.it

[35] Bland JM, Altman DG, *"Statistical methods for assessing agreement between two methods of clinical measurement"* Lancet. 1986; vol 1: pp. 307-310.

[36] Ruggeri A, Scarpa F, Grisan E, McLaren JW, Erie JC, Bourne WM, *"Evaluation of automatic corneal nerve tracing in normal and refractive surgery subjects"* Investigative Ophthalmology & Visual Science. Fort Lauderdale, 2007.

[37] Dani P, Chaudhuri S, *"Automated assembling of images: image montage preparation,"* Pattern Recognition, 1995, vol. 28, nr 3, pp. 431–445.

[38] Scarpa F, Fiorin D, Ruggeri A, *" In Vivo Three-Dimensional Reconstruction of the Cornea from Confocal Microscopy Images"* Proc. 25th Annual International Conference of IEEE EMBS, Lyon, 2007; pp. 747–750.

[39] Otsu N, *"A threshold selection method from gray-level histograms"*, IEEE Transactions on Systems, Man and Cybernetics.1979; vol 9, pp. 62–66.

[40] Ruggeri A, Scarpa F, *"Automatic estimation of keratocyte density in confocal microscopy of the cornea"* Investigative Ophthalmology & Visual Science. Fort Lauderdale, 2008.

[41] Robb RA, "*Visualization in biomedical computing"*, Parallel Computing, 1999; vol 25, pp 2067-2110.

[42] Kundur D, Hatzinakos D, "*Blind image deconvolution,",* IEEE Signal Processing Magazine, May 1996; pp 43-46.

[43] Xu C, Prince JR, *"Gradient vector flow: a new external force for snakes"* IEEE Proc. Conference on Computer Vision and Pattern Recognition, 1997; pp 66-71.

[44] Corkidi G, Marquez J, Usisima R, Toledo R, Valdez J, Graue E, *"Automated in vivo and online morphometry of human endothelium"* Medical & Biological Engineering & Computing, 1993; vol. 31, nr. 4, pp. 421–426.

[45] Sanchez-Marin FJ, *"Automatic segmentation of contours of corneal cells,"* Computers in biology and medicine, 1999; vol. 29, pp. 243–258.

[46] Foracchia M, Ruggeri A, *"Cell contour detection in corneal endothelium In-Vivo microscopy"* Proc. Chicago 2000 – World Congress on Medical Physics and Biomedical Engineering, 2000; pp 1033-1035.

[47] Gain P, Thuret G, Kodjikian L, Gavet Y, Turc PH, Theillere C, Acquart S, Le Petit JC, Maugery J, Compos L, *"Automated tri-image analysis of stored corneal endothelium"* British Journal of Ophthalmology, 2002; vol. 86, pp. 801–808.

[48] Oblak E, Doughty MJ, Oblak L, *"A semi-automated assessment of cell size and shape in monolayers, with optional adjustment for the cell–cell border width—application to human corneal endothelium"* Tissue & Cell, 2002; vol 34, nr 4, pp 283–295.

[49] Foracchia M, Ruggeri A, *"Corneal endothelium analysis by means of bayesian shape modeling"* Proc. 25th Annual International Conference of IEEE EMBS, 2003; pp. 794–797.

[50] Hasegawa A, Itoh K, Ichioka Y, *"Generalization of shift invariant neural networks image processing of corneal endothelium"* Neural Networks, 1996; vol 9, nr 2, pp 345-356.

[51] Zhang W, Hasegawa A, Itoh K, Ichioka Y *"Image processing of human comeal endothelium based on a learning network"* Applied Optics, 1991; vol 30, nr 29, pp 4211-4217.

[52] Chang CI, Du Y, Wang J, Guo SM, Thouin PD *"Survey and comparative analysis of entropy and relative entropy thresholding techniques"*, Proc. Vision, Image and Signal Processing, 2006; vol 153, nr 6, pp 837-850.

[53] Prydal JI, Franc F, Dilly PN, Kerr Muir MG, Corbett MC, Marshall J, *"Keratocyte density and size in conscious humans by digital image analysis of confocal imagse"* Eye, 1998; vol 12, pp 337-342.

[54] Patel SV, McLaren JW, Camp JJ, Nelson LR, Bourne WM, *"Automated quantification of keratocyte density by using confocal microscopy in vivo"* Investigative Ophthalmology & Visual Science, 1999; vol 40; nr 2, pp 320-326.

[55] McLaren JW, Patel SV, Nau CB, Bourne WM, *"Automated assessment of keratocyte density in clinical confocal microscopy of the corneal stroma"* Journal of Microscopy, 2008; vol 229, pp 21-31.